

INVESTIGATING THE PHYSICAL PROPERTIES OF FeCu AND ITS  
POTENTIAL USE IN DYE SENSITIZED  
SOLAR CELLS

by

Mariam Yousif Yousif AlAwadhi

A Thesis Proposal Presented to the Faculty of the  
American University of Sharjah  
College of Engineering  
in Partial Fulfillment  
of the Requirements  
for the Degree of  
  
Master of Science in  
Mechanical Engineering

Sharjah, United Arab Emirates

July 2021

## **Declaration of Authorship**

I declare that this thesis is my own work and, to the best of my knowledge and belief, it does not contain material published or written by a third party, except where permission has been obtained and/or appropriately cited through full and accurate referencing.

Signature (Mariam Yousif Y. AlAwadhi).....

Date: July 9, 2021

The Author controls copyright for this report.  
Material should not be reused without the consent of the author. Due  
acknowledgement should be made where appropriate.

© Year 2021

Mariam Yousif Yousif AlAwadhi

ALL RIGHTS RESERVE

## Approval Signatures

We, the undersigned, approve the Master's Thesis of Mariam Yousif Y. AlAwadhi

Thesis Title: Investigating the Physical Properties of FeCu and its Potential use in Dye Sensitized Solar Cells

Date of Defense: July 6, 2021

### Name, Title and Affiliation

### Signature

---

Dr. Wael Abuzaid  
Associate Professor, Department of Mechanical  
Engineering  
Thesis Advisor

---

Dr. Abdul Hai Al Alami  
Professor, Department of Sustainable and Renewable  
Energy Engineering (University of Sharjah)  
Thesis Co-Advisor

---

Dr. Maen AlKhader  
Associate Professor, Department of Mechanical  
Engineering  
Thesis Committee Member

---

Dr. Mehmet Egilmez  
Associate Professor, Department of Physics  
Thesis Committee Member

---

Dr. Mamoun Fahed Saleh Abdel-Hafez  
Head  
Department of Mechanical Engineering

---

Dr. Lotfi Romdhane  
Associate Dean for Graduate Affairs and Research  
College of Engineering

---

Dr. Sameer Al-Asheh  
Interim Dean  
College of Engineering

---

Dr. Mohamed El-Tarhuni  
Vice Provost for Research and Graduate  
Studies Office of Graduate Studies

## **Acknowledgment**

First and foremost, I would like to express my sincere and deep gratitude to those who contributed towards the completion of my degree.

In particular, my advisor Dr. Wael Abuzaid, who has guided and supported me through this long and challenging journey and has pushed me towards achieving my maximum potential. Thank you for all the wisdom and knowledge you've shared.

Dr. Mehmet Egilmez, who has always shown keen interest, support, and encouragement towards this work. Thank you for all your efforts

Dr. Abdul hai Al Alami, who has given me a new insight towards renewable energy and has been my mentor for the last six years. Thank you for your wisdom

My professors at the Mechanical Engineering department, thank you for all the knowledge you've share and support you've shown, you have my deepest respect and gratitude.

I would like to thank Eng. Adnan Alachkar and Eng. Shamma Saqir who have put important effort into the accomplishment of the project.

To my family and friends, thank you for your continuous love and support, without your encouragement through these rough times it would not have been possible.

To my Dubai Police family, thank you for the support and faith you've put in me. Especially Major Dr. Rawdha AlShamsi and Captain Dr. Rashid Almansoori who helped me during the final stages of this journey

## **Dedication**

*To my family...*

## Abstract

The development of solar cells has revolutionized the renewable energy sector and still holds significant potential for further advancements. Different solar cell technologies have been proposed and utilized in practical applications. This work is focused on the special class of dye-sensitized solar cells which have been developed with the aim of achieving lower cost and higher cell efficiencies. The flexibility and simplicity of these photo-electrochemical systems has motivated significant research efforts in this field. Current efforts are focused on the utilization of alternative materials to replace the rather expensive platinum electrodes. The physical properties of the Iron-Copper system present an appealing choice as an alternative counter-electrode material. However, due the complexities in preparing metastable Fe-Cu alloys, the understanding of the fundamental electrical properties of this system remains limited and not fully understood. Developing a better understanding of the electrical properties of Fe-Cu, including composition dependencies, are relevant to the potential use of this alloy system in solar cell applications. In this work,  $\text{Fe}_x\text{Cu}_{100-x}$  alloys where  $x$  (wt%) = 25, 35, 50, 65, and 75 were prepared via mechanical alloying (MA) method. Microstructural characterization revealed a single-phase face-centered cubic structure for a wide range of compositions. Temperature dependencies of the resistivity were measured for all samples. At low temperatures, the  $\text{Fe}_{25}\text{Cu}_{75}$  alloy exhibited  $T^{3/2}$  dependence of the resistivity. At higher temperatures (100-300K) all of the mechanically alloyed Fe-Cu exhibited unusual  $T$  linear dependence resistivity. As for the magnetic properties, samples with Fe content higher than 35% exhibited magnetic transition temperatures ( $T_c$ ) higher than 350K. The counter-electrode was manufactured by depositing  $\text{Fe}_{50}\text{Cu}_{50}$  on an aluminum sheet using MA and rolling methods. Dye-sensitized cells were produced, assembled, and tested with both platinum electrodes and Al- $\text{Fe}_{50}\text{Cu}_{50}$  counter electrodes, resulting in maximum efficiencies of (3.7%) and (0.26%) respectively. Additionally, the efficiency-cost of these cells were investigated resulting in (0.25% per AED) for platinum electrode, and (3.0% per AED) for Al- $\text{Fe}_{50}\text{Cu}_{50}$  electrode. The obtained results indicate that it has a notable potential which warrants further research and optimization efforts.

**Keywords:** *Photovoltaic, Dye Sensitized Solar Cells, Fe-Cu, Mechanical Alloying, Electric Transport, Magnetization Properties, Efficiency-Cost Analysis*

## Table of Contents

Abstract.....	6
List of Figures .....	9
List of Tables .....	11
Chapter 1. Introduction .....	12
1.1. Overview .....	12
1.2. Research Contribution.....	15
1.3. Research Objectives .....	15
1.4. Thesis Organization.....	16
Chapter 2. Literature Review .....	17
2.1. Drivers of Change .....	17
2.2. Renewable Energy.....	18
2.3. Photovoltaic Energy .....	20
2.3.1. History. ....	20
2.3.2. Solar cells – basic concept.....	21
2.4. Third Generation Solar Cells.....	23
2.4.1. Dye-sensitized solar cells .....	25
2.4.2. Organic photovoltaics (OPVs).....	26
2.4.3. Inorganic photovoltaics (CZTSSe).....	26
2.4.4. Quantum dot–sensitized solar cell (QDSSC) .....	26
2.4.5. Perovskite solar cells .....	26
2.5. Iron-Copper System as an alternative counter-electrode .....	27
2.5.1. Iron (Fe) alloys .....	27
2.5.2. Iron-copper alloy .....	28
Chapter 3. Methodology .....	31
3.1. Preparation of Fe <sub>x</sub> Cu <sub>100-x</sub> .....	31
3.1.1. Materials .....	31
3.1.2. Equipment and experimental procedure .....	31
3.3. TiO <sub>2</sub> Photoelectrode .....	35
3.3.1. Materials .....	35
3.3.2. Equipment preparation .....	35
3.3.3. TiO <sub>2</sub> mesoporous layer .....	36
3.4. Dye-Sensitized Solar Cell Assembly and Testing.....	37
Chapter 4. Results and Discussion.....	40
4.1. Scanning Electron Microscope (SEM) & EDX .....	40
4.2. Energy Dispersive X-Ray (EDX).....	40
4.3. X-Ray Diffraction (XRD) .....	42
4.3.1. Electrical properties .....	44
4.3.2. Magnetization properties .....	47
4.3.3. Magnetoresistance. ....	49

4.4. Counter electrode analysis .....	50
4.5. Cell Testing .....	53
4.6. Motivation for the use of Fe-Cu .....	56
Chapter 5. Conclusion.....	58
6. References.....	61



## List of Figures

Figure 1: Energy Production World Trend 1990-2019 [59] .....	17
Figure 2: Global Renewable Energy Capacity Investment, 2004 to 2019, \$BN [61] .	19
Figure 3: Global Investment in Renewable Energy Capacity by Sector in 2019, and Growth on 2018, \$BN [61] .....	19
Figure 4: Site-Specific Solar Energy Yield Estimates [62] .....	20
Figure 5: Photovoltaic Power Potential - United Arab Emirates [63] .....	20
Figure 6: Simplified timeline of earlier photovoltaics development [66].....	21
Figure 7: Current voltage (IV) cure of a solar cell [70].....	22
Figure 8: Best Photovoltaic Research-Cell Efficiencies - National Renewable Energy Laboratory [10] .....	23
Figure 9: Energy level diagram in DSSCs with graphene electron transport layer [13] .....	25
Figure 10: Schematic diagram of dye-sensitized solar cells [78] .....	25
Figure 11: Calculated phase diagram of Fe-Cu [102].....	29
Figure 12: Progressive XRD spectra of milled powder, for Fe <sub>50</sub> Cu <sub>50</sub> [103].....	30
Figure 13: Mechanical Press .....	32
Figure 14: Fe <sub>x</sub> Cu <sub>100-x</sub> Pellets .....	32
Figure 15: MPP's iBond 5000 Manual Wedge Bonder .....	32
Figure 16: Fe <sub>x</sub> Cu <sub>100-x</sub> after soldering wires onto it to load into the Cryogen System..	32
Figure 17: Cryogen-Free Measurement System .....	33
Figure 18: Deposition of Fe <sub>50</sub> Cu <sub>50</sub> on Aluminum Sheet using Retsch PM 100 planetary ball mill .....	34
Figure 19: Flattening the Al-FeCu electrode using the HK Malvi Wire Sheet Roller	35
Figure 20: TiO <sub>2</sub> nanocrystalline powder .....	36
Figure 21: Addition of PEG to the TiO <sub>2</sub> .....	36
Figure 22: Annealing of TiO <sub>2</sub> at 450°C.....	36
Figure 23: Overnight Dye-loading in dark area .....	37
Figure 24: Cells after cleaning and insulating .....	37
Figure 25: Assembled Dye-Sensitized Cell .....	37
Figure 26: Schematic of the cell using Fe <sub>50</sub> Cu <sub>50</sub> .....	37
Figure 27: Solar Cell Testing Set-up .....	38
Figure 28: Callibration of the ScienceTech Solar Simulator using RERA Solutions Reference Cell.....	39
Figure 29: (a) SEM micrograph images for the prepared Fe <sub>65</sub> Cu <sub>35</sub> powder. (b) higher magnification image.....	40
Figure 30: EDX maps of a single Fe <sub>65</sub> Cu <sub>35</sub> particle, (a) displays EDS layered image of a single Fe <sub>65</sub> Cu <sub>35</sub> particle (b) indicates the Iron composition and distribution in that particle, (c) indicates the Copper composition and distribution, and measure chemical composition provides the exact weight percentage of Iron and Copper in a single Fe <sub>65</sub> Cu <sub>35</sub> particle.....	41
Figure 31 (a)-(g): X-ray diffraction patterns for synthetized Fe <sub>x</sub> Cu <sub>100-x</sub> alloys. Measured spectrums from Fe and Cu starting material are included for ease of comparison. Peaks belong to a bcc phase are marked as B and peaks assigned to the fcc structure are marked .....	43
Figure 32: The lattice parameters as a function of Fe fraction in studied Fe <sub>x</sub> Cu <sub>100-x</sub> system .....	44

Figure 33 (a)-(e): Temperature dependence of the resistivity for all ball-milled alloys. Residual resistivity ratio (RRR) and residual resistivity ( $\rho_0$ ) are shown for each sample. The linear dashed lines are guides for the eye. ....	45
Figure 34 (a)-(d): Temperature dependence of the resistivity of Fe <sub>25</sub> Cu <sub>75</sub> and Fe <sub>50</sub> Cu <sub>50</sub> alloys .....	47
Figure 35: (a) Temperature dependence of the zero-field cooled (ZFC) mass magnetization for all mechanically alloyed specimens. The magnetization data for Fe starting powder has been also presented for comparison. (b) Temperature dependence of the magnet, (d) The lattice parameters as a function of Fe fraction in studied Fe <sub>x</sub> Cu <sub>100-x</sub> system.....	49
Figure 36: Magnetic field dependence of the resistivity for mechanically alloyed Fe <sub>x</sub> Cu <sub>100-x</sub> .....	50
Figure 37: SEM of Rolled Al-Fe <sub>50</sub> Cu <sub>50</sub> Sheet used as counter electrode at different magnifications (a) at view field of 1.32mm, (b) at view field of 543 $\mu$ m, (c) 269 $\mu$ m, and (d) 92.3 $\mu$ m view field .....	51
Figure 38 (a)-(e): EDX maps of a single Fe <sub>50</sub> Cu <sub>50</sub> particle embedded into the Aluminum sheet .....	52
Figure 39: EDX maps of an Fe <sub>50</sub> Cu <sub>50</sub> particle embedded into the Aluminum sheet, (a) is an electron image, (b) is the EDS layer image of the particle and its surroundings, (c) is the copper concentration and distribution, (d) indicates iron concentration and distribution, (e) indicates the aluminum concentration and distribution surrounding the particle .....	52
Figure 40: Current-Voltage Curve of Cell 05 .....	56
Figure 41: Power-Voltage Curve of Cell 05 .....	56

## List of Tables

Table 1: Iron and Copper Mass measurement for each target composition .....	31
Table 2: Target composition and the EDX results for each $\text{Fe}_x\text{Cu}_{100-x}$ alloy.....	42
Table 3: Dye-Sensitized Solar Cell Testing Results using Platinum as a Counter Electrode.....	54
Table 4: Dye-Sensitized Solar Cell Testing Results using $\text{Fe}_{50}\text{Cu}_{50}$ deposited onto an Aluminum sheet as a Counter Electrode .....	55
Table 5: Efficiency–Cost analysis of Cell 08 .....	57

## Chapter 1. Introduction

### 1.1. Overview

Over the last few decades, humanity has witnessed a spike in population with numbers increasing from approximately 3.034 billion people in 1960, to more than 7.7 billion people in 2019. These numbers are projected to grow to around 8.5 billion in 2030, 9.7 billion in 2050, and 10.9 billion in 2100 [1], [2]. The energy demand has increased significantly due to population growth and is expected to amplify in the upcoming years. Therefore, the supply in the energy market is required to match this continuously increasing demand at a low cost and with limited environmental impact. In addition, the inevitable depletion of conventional resources necessitates finding alternative energy sources that can satisfy the global energy needs. This objective has been a critical goal since the third industrial revolution [3]. Not only a drop in conventional energy sources is expected in the years 2030-2040 [4], but a catastrophic long-term effect on the Earth atmosphere is predicted with the prolonged production of greenhouse gases. Countering the effects of high concentration of greenhouse gases in the atmosphere has never been more critical. These conditions emphasize on the importance of research investment in the field of renewable energy, and specifically Dye-Sensitized Solar Cells (DSSC) that contributes towards generating low-cost, green energy. This work adds value to the DSSC field by investigating alternative cost-effective materials that can replace existing commercial or commonly used products in the DSSC structure.

With this increase in demand, combined with the essential need to lower the emission of greenhouse gasses, developing clean, stable, and reliable alternative energy sources is vital. Sustainable and renewable energy production comes in different forms; solar, biomass, wind, tidal, geothermal, etc. [5]. In the United Arab Emirates, where solar energy is abundant due to its geographical location, solar energy can be utilized using several methods such as solar thermal and photovoltaic (PV). The production of electricity directly in plants such as the Mohammed bin Rashid Al Maktoum Solar Park located in Dubai, which is a photovoltaic plant [6]. Solar thermal power plants such as Abu Dhabi's Shams Solar Power Station, use concentrated solar power plant that generates and feeds 100MW electricity into the national grid [7], [8].

With this abundance of solar energy, utilizing this privilege by exploring innovative emerging solar technologies, such as DSSC and perovskites is crucial. Dye-

sensitized solar cells, an emerging technology in solar energy, generates current when a photon is absorbed by a dye-molecule on the n-type material (e.g., Titanium Dioxide) [9]. The initial cells showed a conversion yield of around 7% [9] while more recent and optimized attempts have demonstrated values reaching 13% [10]. Despite the research and development efforts, the efficiency remains limited. The introduction of different materials to replace the conventionally used electron transport layer (ETL), hole transport layer (HTL), photosensitizer, mesoporous layer, compact layer, etc., present a significant room to improve the efficiency of the cells. Due to the fact that dye-sensitized solar cells are photoelectrochemical cells, many limitations may arise as a result of the chemical reactions that occur in the process. The incompatibility of materials, wide bandgaps that may limit the electron transfer, and leakage while using liquid-based electrolytes [11]–[18], oxidation of the material, injection and recombination limitations [19], are some limitations that effect the performance of the DSSC . The simple concept of this cell with its low-cost and high efficiency selling point have played a factor in the selection of this thesis topic and finding methods to enhance this existing technology by introducing new materials aimed at improving the resulting cell performance

In general, the structure of DSSC is complex and includes multiple layers and the use of different materials, the basic DSSS consists of a photoelectrode (a combination of a conducting substrate and a semiconductor active layer), electrolyte, active layer, counter-electrode [20]. This works aims to improve the efficiency of conventional inorganic dye-sensitized solar cells by exploring alternative counter-electrode materials. The study is considering the cell's elements as building blocks that can be easily removed and replaced by other compatible materials. These changes can either increase or decrease the cell's performance.

Traditionally, platinum coated fluorine tin oxide (FTO) is the most commonly used counter-electrode. Due to the semi-precious metal's high efficiency, a result of the electrolyte's rapid regeneration at the counter-electrode in the case of DSSC, it may present as an ideal counter-electrode. On the other hand, platinum and its alternative semi-precious are extremely expensive and rare elements, which steered the focus of research towards Earth-abundant elements as a cheaper alternative to the conventionally used counter-electrode [21].

Following these concepts, the Iron-Copper system provided an appealing cost-effective alternative to the conventionally used expensive and rare metals. Therefore, this work will revolve around the Iron-Copper system (Fe-Cu) as a potential counter-electrode material to substitute the frequently used semi-precious counter-electrode, platinum. Due to their wide range of magnetic properties as a results of various processing conditions, Iron alloys are one of the most important alloys [22]. Recent findings prove a new phenomenon where superconductivity, ferromagnetism[23], [24], and spin glass behavior[25] coexists together in magnetic systems such as Iron. Although stable Fe at room temperature and atmospheric pressure has a body centered cubic (bcc) crystal structure (with lattice parameter  $a$  roughly  $2.87\text{\AA}$ , commonly known as  $\alpha$ -Fe phase), a monoatomic face centered cubic (fcc) Iron ( $\gamma$ -Fe phase, with lattice parameter  $a$  around  $3.54\text{\AA}$ ) can be stabilized directly by substituting Iron atoms with materials characterized by a lattice parameter comparable to that of the  $\gamma$ -Fe lattice parameter (i.e.  $3.5\text{\AA} - 3.6\text{\AA}$ ) [26]. Copper, a nonmagnetic material with an fcc lattice parameter  $a$  approximately  $3.6\text{\AA}$  is selected in this study as the material used to stabilize Iron fcc. Combined with the high conductivity and high strength properties found in Cu-based compounds [27] and compatibility, Iron-Copper alloy make a logically appealing choice. However, the major drawback of such studies is the bulk miscibility of Cu in both  $\gamma$ -Fe and  $\alpha$ -Fe.

Traditionally, iron alloys can be produced by exercising different techniques that control the type and quantity of the alloying elements [28], but due to the limited miscibility between iron and copper elements, the synthesis of single phase Fe-Cu has been a challenge [29], [30]. Nevertheless, sample preparation methods such as magnetron sputtering [30], electrodeposition [31], and mechanical alloying [32], have yielded the required results in alloying Fe and Cu. The mechanical alloying (MA) method has gained a popularity since it was first invented in the 20<sup>th</sup> century JS Benjamin [33], [34]. A solid-state powder alloying technique that was originally developed to produce homogeneous, uniform materials. The technique relies on a repeated process of cold welding, fracturing, and re-welding of the powders using a high energy ball mill [33], [35]–[37]. The process is used to synthesize metastable materials [36] such as supersaturated solid solutions [38], intermediate phases [39], quasi-crystalline materials [29], [40], amorphous alloys [41], and high-entropy alloys [42]. Utilizing this technique to produce Iron-Copper alloys, this study will focus on

the electrical transport properties of the Fe-Cu system, and specifically analyzing the temperature dependence of the resistivity of the system. The operating temperature plays a crucial role in the conversion process of a photovoltaic cell [43]. Therefore, it is important to investigate the effect of temperature on the electrical conductivity of the Fe-Cu system [44], [45], and while focusing on the temperature evolution of resistivity of the Fe-Cu system. Shedding further insight into the physical properties of Fe-Cu enables us to understand its compatibility and practicality in the field of Dye-Sensitized Solar Cells, and specifically for the commercial use at locations with elevated temperatures, such as the United Arab Emirates (U.A.E).

## **1.2. Research Contribution**

Dye-sensitized solar cell's attractiveness is attributed to their cost-effective properties. Over the years, different approaches have been taken to achieve that goal. Research in this field has focused on utilizing materials that have low cost and high efficiencies; such as certain organics dyes and synthetic dyes [12], [13], [46], [47], or replacing the standard photoelectrodes or counter electrodes with alternative cost-effective materials [48]–[50]. In this study, we will be utilizing the mechanical alloying process to produce Iron-Copper alloys of different percentages, investigate their electrical transport properties, and analyzed the temperature dependence of the resistivity of the Fe-Cu system in detail, as a replacement of the Fluorine doped Tin Oxide (FTO), or the expensive platinum counter–electrodes used in as the p-type hole-transport material (HTM). This allows us to utilize Iron-Copper alloy as an effective counter-electrode in a standard dye-sensitized solar cell and compare its performance to the traditionally used platinum electrode.

## **1.3. Research Objectives**

With this target set, the following objectives will be achieved:

1. Develop a benchmark to the dye-sensitized solar cell by producing standard cells as a reference, this will enable us to compare the effectiveness of adding Fe-Cu to the cell.
2. Produce Iron-Copper powders at different compositions by utilizing the Mechanical Alloying method and categorize the crystal structures for each composition respectively.
3. Investigate the magnetic and electrical transport properties of mechanically alloyed  $\text{Fe}_x\text{Cu}_{100-x}$ , system

4. Investigate the electrical conductivity of the Fe-Cu system, while focusing on temperature evolution of resistivity of the Fe-Cu system.
5. Integration of Iron-Copper as an alternative for the platinum electrode, as a counter electrode material.
6. Obtain the characteristic properties of the cells discussed above (efficiency, open-circuit voltage, short-circuit current density, and fill factor).

#### **1.4. Thesis Organization**

The information available in the current document can be accessed as followed: the global impact of existing energy sources and the importance of converting to green energy will be discussed in chapter 2. The concept of third generation solar cells will be introduced, while focusing on dye-sensitized solar cells (DSSC). In addition, we will introduce the operation mechanism and characterization of DSSC cells. Followed by the focus of the study; the Iron-Copper alloy system. The Fe-Cu alloy section will discuss existing works on the system, and their contribution to the study. In chapter 3, the experimental methods and characterization techniques used will be further clarified. Followed by chapter 4, which will revolve around the results and discussion of the experimental work conducted. Finally, chapter 5 provides a summary and conclusion of the work.



## Chapter 2. Literature Review

### 2.1. Drivers of Change

For the past eight hundred thousand years, the levels of carbon dioxide in the atmosphere have fluctuated continuously, following a natural cycle, but never exceeding 300ppm [51]. In the last century, the concentration of carbon dioxide –a greenhouse gas– surged in the atmosphere beginning an unexpected chain reaction which we are currently witnessing. These number are only expected to continue to rise.

As of the latest data available, 86.95% of the world energy produced in 2018 is from fossil fuels sources [52], [53]. This contributes towards the global emission of 33.3Gton CO<sub>2</sub>e [54], [55]. In turn, this resulted in global temperatures in 2018 being 1.5C higher than the mean global temperatures between 1951 and 1980, a considerable amount from the Carbon Budget 2°C [56]. This is considered extremely alarming and requires concentrated efforts to reduce and control emissions. For example, the Paris Agreement was signed in 2016 in order to control the global temperature rise. This is conducted by managing CO<sub>2</sub> emission, maintaining global temperature rise below 2°C by 2025 or 2030, and pursuing efforts that would limit the temperature increase even further to 1.5°C through technological advances [57], [58]. This task has not been made easy with the current global population.

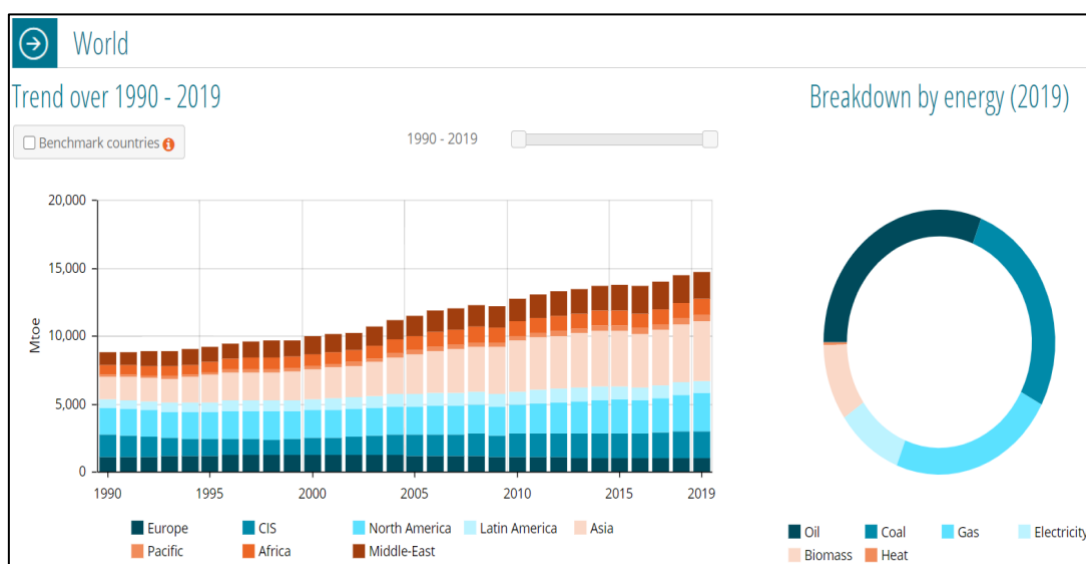


Figure 1: Energy Production World Trend 1990-2019 [59]

As can be observed in Figure 1, the world's dependence on conventional energy has been on the rise which is an expected outcome of population and technological

growth over time. In 2019, the U.S. and China, contributed towards a significant growth in crude oil production and coal production, respectively. Producing a total of 2,303 Mtoe (U.S.), and 2,684 Mtoe (China), each. This has resulted in a substantial increase in global energy production that year. In addition, just these two countries consumed a collective amount of 5,497 Mtoe in 2019 [59], [60].

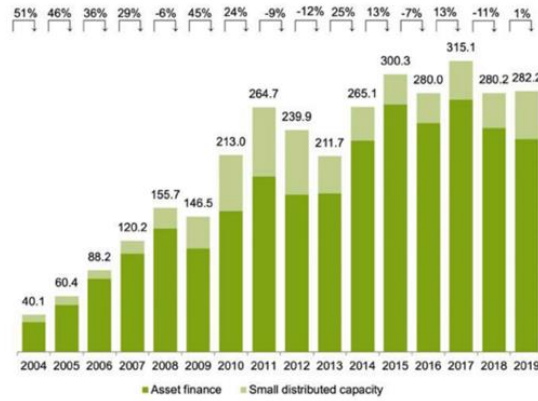
Without even looking at the environmental and economic impact of continuing use of conventional energy sources, understanding that these resources will eventually be depleted is important. Comprehending this predicament and recognizing that communities, cities, and countries can no longer rely on the current conventional sources due to their lack of sustainability and their measurable negative effect on the environment, a change towards a more “clean”, sustainable, and renewable energy sources is finally due. With existing various options in the renewable energy sector, realizing that solar energy is an ideal choice for locations like the United Arab Emirates, is the first step towards achieving energy sustainability.

## **2.2. Renewable Energy**

With the depletion of conventional energy sources, we are currently in a race against time to find efficient, reliable and abundant sources of energy. Therefore, investing in renewable energy has never been more crucial. Renewable Energy is obtained from natural sources or processes with the ability to be constantly replenished, such as; solar energy, wind energy, hydropower, geothermal, and biomass; dubbing renewable energy as “Clean Energy” [18], [23].

Although renewable energy is viewed as a new form of technology, living beings have been utilizing these sources of energy since the dawn of time. Depending on the Sun to provide light, heat, and energy for natural process. Wind to power boat sails and windmills to grind the grain. Biomass through wood to cook food and keep ourselves warm in the cold.

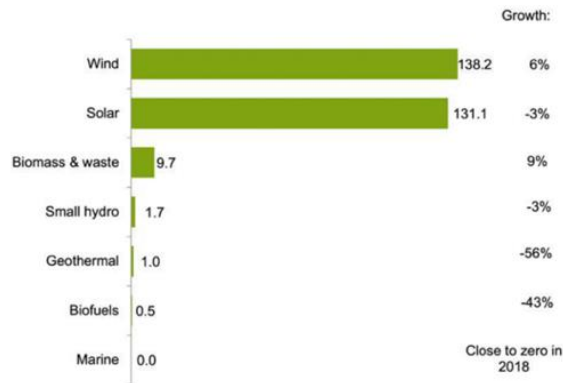
With this approach to converting from conventional energy sources and systems, to renewable and sustainable energy systems comes a huge investment. In 2019, a total of \$282.2 billion was globally invested in the renewable energy sector [61]. The global renewable energy investment trend can be seen in Figure 2.



Total values include estimates for undisclosed deals  
 Source: UNEP, Frankfurt School-UNEP Centre, BloombergNEF

Figure 2: Global Renewable Energy Capacity Investment, 2004 to 2019, \$BN [61]

Realizing the importance of this investment, it can be seen in Figure 3 the amount of money invested in each type of renewable energy source globally in 2019 and their growth in comparison to the year 2018. As can be noticed. Solar energy was the second most-invested in field of renewable energy in 2019.



Total values include estimates for undisclosed deals.  
 Source: UNEP, Frankfurt School-UNEP Centre, BloombergNEF

Figure 3: Global Investment in Renewable Energy Capacity by Sector in 2019, and Growth on 2018, \$BN [61]

Although wind energy takes the lead when it comes to investment in the field of renewable energy, the United Arab Emirates' geographical location has high photovoltaic power potential as can be seen in Figure 4 and

Figure 5, where the specific photovoltaic power output is clearly noticeable at 5.12kWh/kWp, a clear indication that this site is more suitable for photovoltaic energy due to its abundant incoming solar flux. This is a great indicator to invest in the \$131.1 billion dollars were invested in that field of renewable energy [61]–[63].

The utilization of solar energy can be completed using different methods of conversion such as solar thermal energy which utilizes the heating up of the working fluid process for either heating and cooling systems or electrical generation.

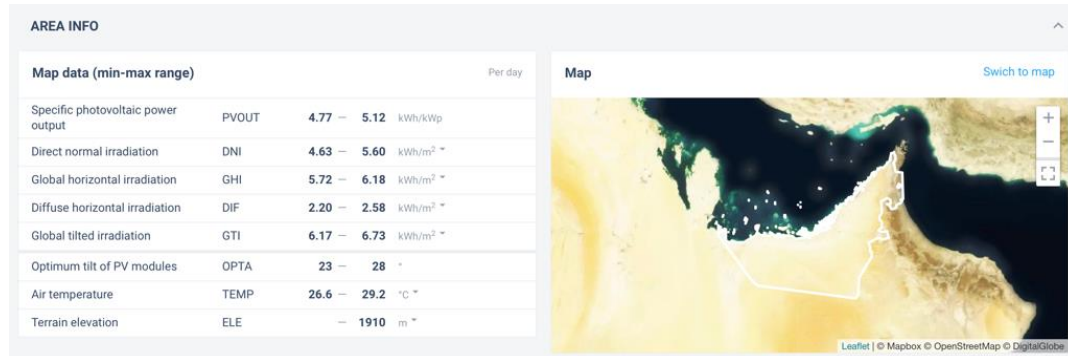


Figure 4: Site-Specific Solar Energy Yield Estimates [62]

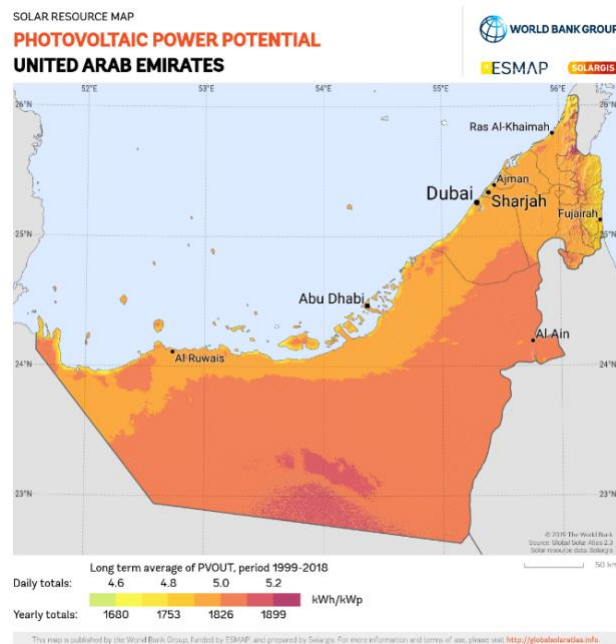


Figure 5: Photovoltaic Power Potential - United Arab Emirates [63]

## 2.3. Photovoltaic Energy

**2.3.1. History** In 1839, and at the age of 19, Alexandre Edmond Becquerel was able to create and analyze the world’s first photovoltaic cell. The first photovoltaic cell consisted of two electrodes placed in an acidic solution, that is separated by a thin membrane. When illuminating one of these electrodes, Becquerel was able to observe an electrical generation [64], [65]. Figure 6 shows a simplified timeline of earlier PV development from the birth of photovoltaics till the first PV in space.

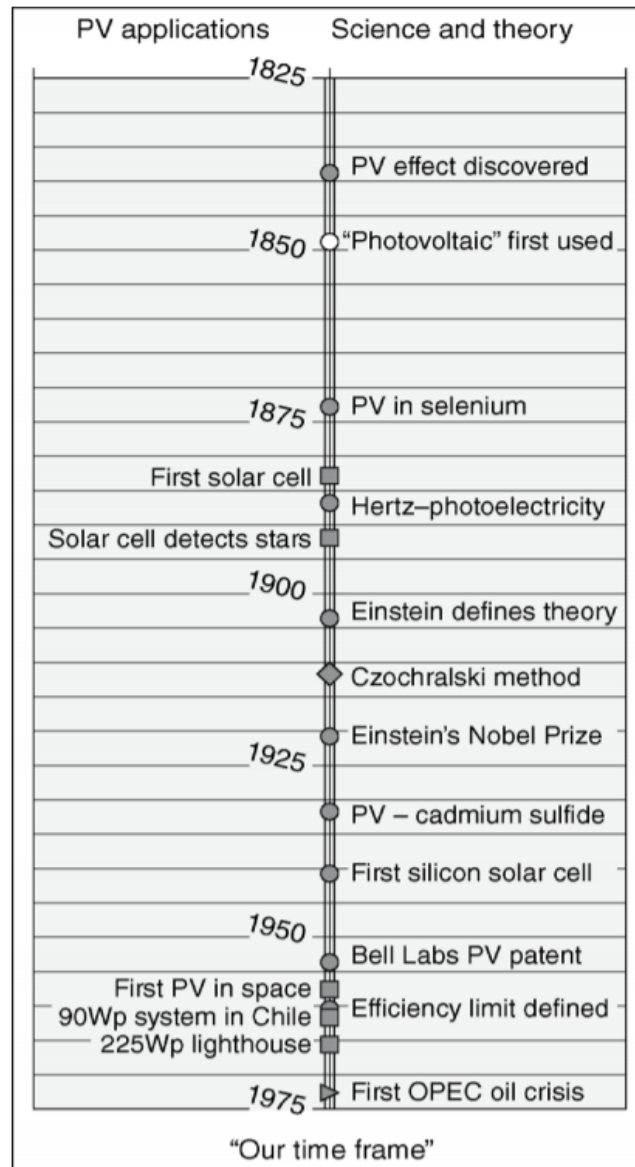


Figure 6: Simplified timeline of earlier photovoltaics development [66]

**2.3.2. Solar cells – basic Concept** Because of the intriguing concept, Solar cells have gained a popularity in the 19<sup>th</sup> century. As Markvart et al. [67] explained it, the photovoltaic energy conversion follows two steps. First, when the incident light hits the cell, photons excite the semiconductor, generating free-carriers (in case of inorganic solar cell) or excitons (in case of organic solar cells) in the semiconductor material by absorbing these photons that have energies higher than their bandgap [68]. Resulting in the creation of an electron-hole pair. This electron-hole pair is then separated into two terminals: holes to the positive terminal, and electron to negative terminal, resulting in electrical power generation.

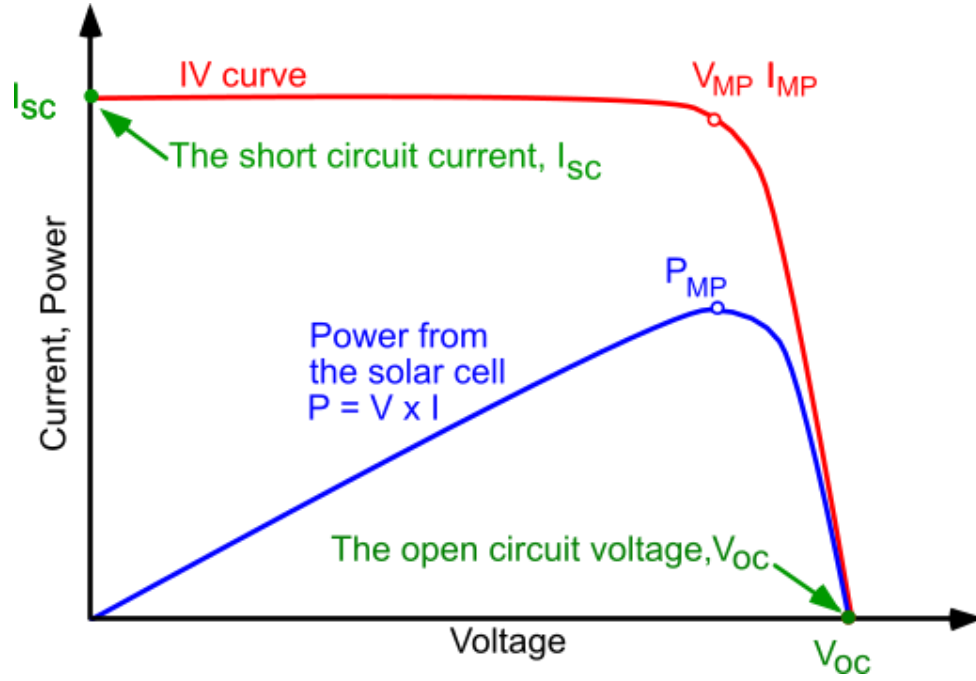


Figure 7: Current voltage (IV) cure of a solar cell [70]

For an ideal solar cell, the current can be calculated using Equation (1) from the Shockley solar equation. Where for an ideal cell the photogenerated current ( $I_{ph}$ ) is equal to the short circuit current ( $I_{sc}$ ), and ( $J_{ph}$ ) is the maximum theoretically achievable value for the short-circuit current density. On the other hand, the for an ideal solar cell, by using Equation (2) we can obtain the open-circuit voltage [67].

$$I = I_{ph} - I_0 \left( e^{\frac{qV}{k_B T}} - 1 \right) \quad (1)$$

$$V_{oc} = \frac{k_B T}{q} \ln \left( 1 + \frac{I_{ph}}{I_0} \right) \quad (2)$$

The solar cell's maximum power ( $P_{max}$ ) can be used to obtain the maximum current ( $I_m$ ), and maximum voltage ( $V_m$ ). Using this definition, and by using Equation (3), we can obtain the cell's fill factor; or the measure of squareness of the I-V curve [69].

$$FF = \frac{P_{max}}{I_{sc} V_{oc}} = \frac{I_m V_m}{I_{sc} V_{oc}} \quad (3)$$

Using these values and the previous equations, the efficiency of the cell can be obtained using Equation (4).

$$\eta = \frac{P_{max}}{Area \times Irradiance (100mW/cm^2)} = \frac{I_{sc}V_{oc} \times FF}{rea \times Irradiance (100mW/cm^2)} \quad (4)$$

Figure 7, shows a graph of the I–V curve of the cell in red, the ( $V_{MP}$ ,  $I_{MP}$ ) point indicates the maximum power of the cell that correspond to the maximum current and voltage. The open–circuit voltage can be seen when the current is zero. As for the short–circuit current, the value is on the y-axis where the voltage is zero.

## 2.4. Third Generation Solar Cells

Over the past years, solar cells have emerged to offer a reliable substitute to conventional energy sources, such as fossil fuels. This in turn, contributes towards providing large amounts of green–energy at affordable prices [71].

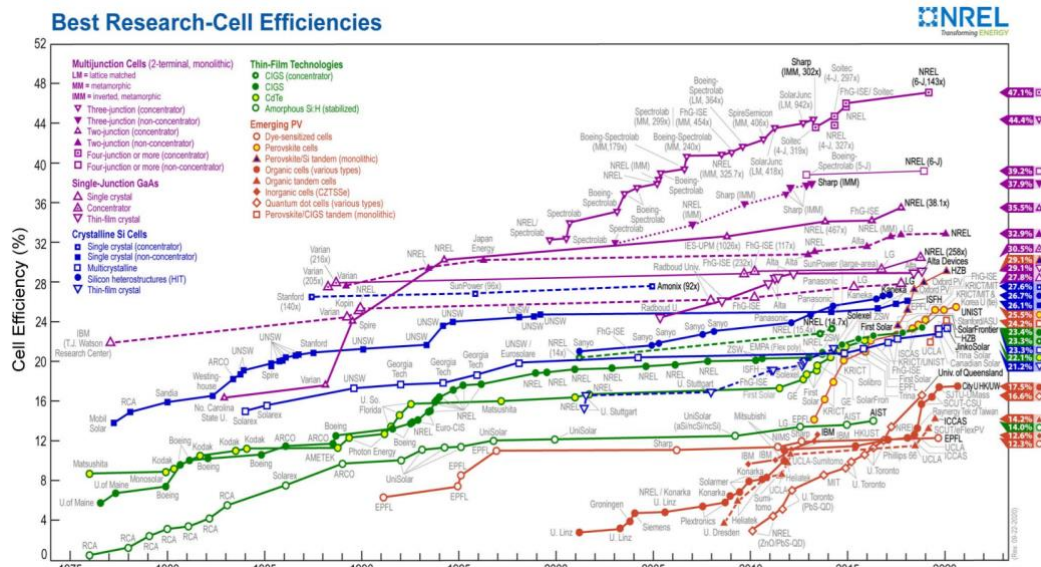


Figure 8: Best Photovoltaic Research-Cell Efficiencies - National Renewable Energy Laboratory [10]

With these technological advances in the photovoltaic field, and specifically the approach of the Shockley-Queisser’s 31–41% power efficiency limit (SQ limit) for single bandgap solar cells [72], [73], studies were conducted to find methods to circumvent the SQ limit. One of resulting findings were third-generation solar cells. Third-generation solar cells are an alternative, nanostructured materials–based devices that aim to enhance the performance of their predecessor (the second-generation technology; thin film), while maintaining the low–cost target. This technology primarily involves organic photovoltaics (OPVs), copper zinc tin sulfide (CZTS), quantum dot–sensitized solar cell (QDSSC), dye-sensitized solar cells (DSSCs), and

perovskite solar cells [68]. Figure 8 illustrates the latest best research-cell efficiencies over the years reported by the National Renewable Energy Laboratory [10].

In certain cases, the end-user would prefer price over electric power production (in case of small applications), and vice-versa. In all situations, the efficiency of the cells guarantees both. High efficiency does not necessarily mean high cost, with high efficiencies, less material is required, and more power is produced. Typically, a solar cell consists of the photoelectrode, a counter electrode, the active area, and an electrolyte. Changing these factors to optimize the price-vs-efficiency properties creates ideal solar cells for different situations.

To understand the importance of these layers we need to understand the operation mechanism of these cells. Since energy is generated from the photons absorbed, the optoelectrical properties of the cell plays a major role in the operation. Where the properties of the photosensitizers (in the case of this thesis; ruthenium dye) are one of the most important factors that determine the performance of the solar cell. Properties such as the absorption of the photosensitizer. With these types of cells broad absorption is usually targeted to utilize the maximum range of the solar spectrum, extending the near infrared region is crucial to achieve that goal and ensuring the production of a large photocurrent which translates to high efficiency [14], [16], [74], [75].

In addition, having these layers facilitate the electron transfer from the Highest Occupied Molecular Orbital (HOMO) to the Lowest Unoccupied Molecular Orbital (LUMO). Due to the gap between these orbital levels, electron transfer from the semiconductor can be hindered, requiring higher energy levels to be absorbed to ensure the excitation of the electrons. Therefore, different technologies were investigated and introduced, to act as a ladder step between these orbital levels causing the bandgap to shrink while ensuring a wide and strong absorption spectra [11]–[17].

To demonstrate this Figure 9 is used as an example to show how the addition of graphene as an electron transport layer (ETL) resulted in shrinking the bandgap which translates to an increase in the short-circuit current density and efficiency as reported by Chen et al. [13]. This is due to graphene containing graphene oxide, which has a large work function range [76], [77], with of 4.9eV reported falling into that range, this work function is similar to that of the ITO used in the experimentation process reported.



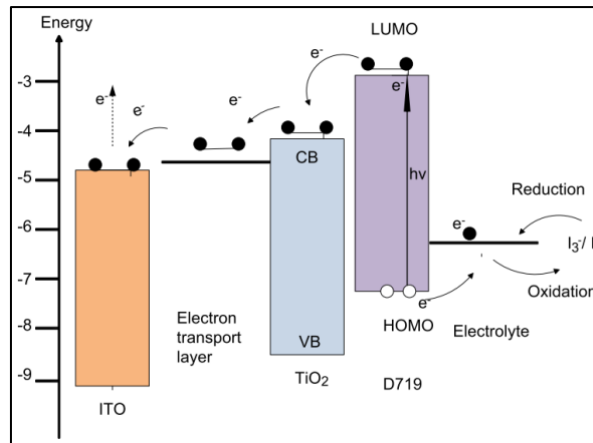


Figure 9: Energy level diagram in DSSCs with graphene electron transport layer [13]

**2.4.1. Dye-sensitized solar cells** More than a century after Becquerel's discovery, in 1991, O'Regan et al. introduced the concept of dye-sensitized solar cells (DSSC). These photoelectrochemical devices left a great impact in the field when O'Regan and Grätzel first used a mesoporous semiconductor electrode with high internal surface area. This mesoporous layer is submerged into a dye and generates a current when a photon is absorbed by a dye-molecule on the n-type material (in this case Titanium Dioxide). Giving a rise to electron injection into the conduction band of the semiconductor. The circuit is then complete when the dye is regenerated by electron transfer from a redox species in the solution that is then reduced at the counter-electrode at the time resulting in a 7.1%-7.9% power conversion efficiency [9], [12], [68]. As seen in Figure 8, the highest achieved efficiency in 2020 stands at 12.3%,

Figure 10 illustrates the architecture of the standard cell, where the LUMO and HOMO can be seen in the figure.

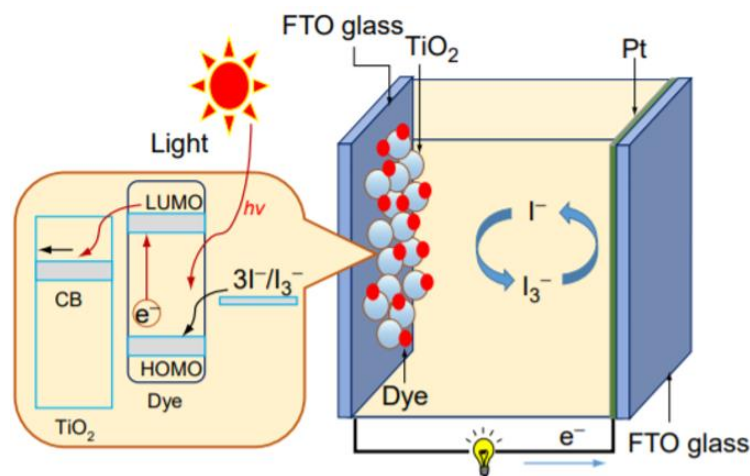


Figure 10: Schematic diagram of dye-sensitized solar cells [78]

**2.4.2. Organic photovoltaics (OPVs)** Bulk–heterojunction organic solar cells were first invented in 1992 by Sariciftci et al., after discovering evidence of electron transfer from the excited state of a conducting polymer onto buckminsterfullerene. After the photo-excitation of the polymer, an electron transfer on to the buckminsterfullerene is initiated [79]. Over the years, this technology developed as can be seen in Figure 8. In 2020, Ma et al. [11] were able to reach 17.52% conversion efficiency by adding 10% of a non-fullerene small molecule acceptor (C8-DTC) to PM6:Y6 system. Resulting in an open-circuit voltage of ( $V_{oc}=0.873V$ ), a short-circuit current density of ( $J_{sc}=26.50 \text{ mA/cm}^2$ ), and a fill factor of ( $FF=75.61\%$ ).

**2.4.3. Inorganic photovoltaics (CZTSSe)** Unlike OPVs, inorganic photovoltaic cells are still far below the SQ limit of 31% efficiency under 1.5AM [72]. Where the highest efficiency achieved was recorded in 2013, by Wang et al. [80], having the efficiency of 12.6%, an open-circuit voltage of ( $V_{oc}=0.5134V$ ), a short-circuit current density of ( $J_{sc}=35.2 \text{ mA/cm}^2$ ), and a fill factor of ( $FF=69.8\%$ ). This was achieved by a hydrazine pure-solution process. Where previously, Gokmen et al. [81], were able to achieve an efficiency of 11.1%, an open-circuit voltage of ( $V_{oc}=0.4598V$ ), a short-circuit current density of ( $J_{sc}=34.5 \text{ mA/cm}^2$ ), and a fill factor of ( $FF=69.8\%$ ).

**2.4.4. Quantum dot–sensitized solar cell (QDSSC)** In 1989, Barnham et al. [82] suggested the usage of quantum wells as the active region in solar cells for photon–absorption in solar cells. This targeted the approach of high-efficiency multi–band gap solar cells. This ignited the curiosity of researchers to participate in developing the QDSSC field. Today, Hao et al. [83], was able to achieve 16.6% efficiency by mixing caesium and formamidine lead triiodide perovskite system in the form of quantum dots by using an effective oleic acid ligand-assisted cation–exchange strategy that allows controllable synthesis of the quantum dots. Resulting in an open-circuit voltage of ( $V_{oc}=1.17V$ ), a short-circuit current density of ( $J_{sc}=18.3 \text{ mA/cm}^2$ ), and a fill factor of ( $FF=78.3\%$ ).

**2.4.5. Perovskite solar cells** In 2009, Kojima et al. [84] studied  $CH_3NH_3PbBr_3$  and  $CH_3NH_3PbI_3$  (lead halide perovskite compounds)’s photovoltaic functions as visible light sensitizers in photoelectrochemical cells. The results from the addition of these solutions to the ordinary dye-sensitized solar cell structure were noticeable in the large optical absorption coefficient, low-cost, low-temperature processing, and high

performance, make perovskites materials a promising candidate for largescale applications in the field of solar power generation [68], [85]. Today, Perovskites were able to overcome many barriers and achieve up to 25.5% efficiency for single-junction architectures, and 29.1% for Perovskite/Silicon tandem cells [10].

## 2.5. Iron-Copper System as an Alternative Counter-Electrode

With these different technologies, exploring various alternatives to the existing techniques and approaches to improve the efficiency and performance of the cell becomes imperative. With the depletion of precious resources, finding Earth-abundant elements as a cheaper alternative to the conventionally used counter-electrode [21] has never been more crucial. Following these concepts, the Iron-Copper system provided an attractive cost-effective alternative to the conventionally used semi-precious and expensive metal.

**2.5.1. Iron (Fe) alloys** Fe-alloys are among the most widely used systems in practical applications. Being cost effective and highly engineerable through alloying (i.e., chemical composition), mechanical processing (e.g., for grain size control), and thermal treatment [28]. At ambient temperature and pressure, Fe is in its most stable form having a body-centered cubic (bcc) crystal structure ( $\alpha$ -Fe) with a lattice parameter of about 2.87 Å [26]. In this  $\alpha$ -form, Fe is ferromagnetic with a Curie temperature ( $T_c$ ) of 1043 K and a saturation magnetic moment of  $\approx 2.2 \mu_B/\text{Fe}$  [86].  $\alpha$ -Fe goes through martensite to austenite structural phase transition at 1183 K where a face-centered cubic (fcc) structure with a lattice parameter of 3.54Å, or more commonly known  $\gamma$ -Fe, is formed [87]. Such  $\gamma$ -Fe phase is only stable at temperatures higher than the magnetic ordering temperature; hence, it is not possible to have stable  $\gamma$ -Fe at ambient temperatures in elemental form.

Even though  $\gamma$ -Fe is not stable at room temperature, revealing the magnetic character of  $\gamma$ -Fe at low temperatures has always been one of the important themes of discussion and debate from both experimental and theoretical points of view in materials science. The Fe-Cu system considered in this work, creates complex and primarily dual phase structures when prepared using traditional casting methods. However, through specifically tailored mechanical alloying methods, which do not rely on melting the constituent elements, the Fe-Cu can be stabilized in fcc form across a wide range of compositions. The fcc stabilized Fe-Cu alloy provides means to shed

further insight into the physical properties of  $\gamma$ -Fe alloys which as noted above is challenging and limited in the literature. In this work, the potential for using this system in DSSC is explored. Some of the relevant physical properties to such an application are thoroughly evaluated, e.g., transport, as part of this investigation.

**2.5.2. Iron-Copper alloy** In practice, the easiest and most reliable way of stabilizing the  $\gamma$ -Fe phase is the substitution of Fe atoms in a stable monatomic fcc crystal lattice whose lattice parameter is similar to that of  $\gamma$ -Fe. In this respect, fcc metals such as Ni, Pt, Pd, and Cu have been used for alloying with Fe. Pt and Pd fcc structures have a lattice parameter of about 3.9Å which are about 10% larger than the  $\gamma$ -Fe [87]. This large difference in lattice parameters leads to a face-centered tetragonal structure and enhancement of the magnetic moment of the Fe compared to its value in pure bcc Fe. On the other hand, the lattice parameters of fcc Ni and Cu are 3.5Å and 3.6Å respectively; therefore, they can be good choices as stable monoatomic fcc host for Fe substitution. Magnetic and mechanical properties of the FeNi system are very rich and heavily studied and utilized in various fields such as microelectronic devices [88], magnetic shielding [89], and construction industries [90]. However, in the FeNi system, both alloy constituents are magnetic hence, complex magnetic interactions between the Fe and Ni atoms bring difficulty in understanding the magnetic properties of the  $\gamma$ -Fe.

On the other hand, when suitably alloyed, ferromagnetic–nonmagnetic alloys present noteworthy saturation magnetization and magnetoresistance. In addition, when these alloys are prepared under carefully measured conditions, they have the ability to form distinct, unique micro and nano structures over a broad temperature range [91].

Fcc Cu, as the host for the Fe, is a good alternative for perceiving the magnetic properties of  $\gamma$ -Fe as Cu is nonmagnetic. However, the major drawback of such studies is the bulk miscibility of Cu in both  $\gamma$ -Fe and  $\alpha$ -Fe is very small, only a few percent at higher temperatures [26], [86], [92]–[94]. Consistent with this solubility of the bulk Fe in Cu is also very low [30]. Nevertheless, the miscibility issues of Fe and Cu have been partially lifted when adapting alternative sample preparation methods such as magnetron sputtering [30], electrodeposition [31], vapor condensation [95], and mechanical alloying [32]. In sputtered or electrodeposited  $\text{Fe}_x\text{Cu}_{100-x}$ , (where  $x$ , is the Fe percentage) single-phase fcc structures for  $0 \leq x < 60$ , bcc single-phase structures

for  $75 \leq x < 100$  and dual phase (fcc+bcc) structures for  $x = 60 - 75$  have been reported [30], [96]. Recently, mechanical alloying has been widely used for the fabrication of single-phase  $\text{Fe}_x\text{Cu}_{100-x}$  alloy. As mentioned above, the nonmagnetic character of Cu makes the Fe-Cu system an important system for understanding the magnetic properties of  $\gamma$ -Fe. The difficulty in obtaining single-phase solid solutions limited the research on this material. However, there are a number of studies on the magnetic properties of Fe-Cu system [26], [86], [92], [97], [98]. These studies mostly concentrate on bulk magnetic moments, invar effect, and collinear magnetism.

Due to compatibility issues between iron and copper elements [29], [30], the processing of the Fe-Cu system is challenging and hard to accomplish using traditional alloying methods, such as casting, which is a method that involves alloying the metals after bringing them to their melting point, and casting them into a mold [28], [99]. The calculated phase diagram of Fe-Cu shown in Figure 11, highlight a clear liquid miscibility gap which indicates that at high temperatures, the two liquids (i.e., Fe and Cu) will not mix[100]. Additionally, with the increase of temperature, the solubility limit of copper in iron increases [101].

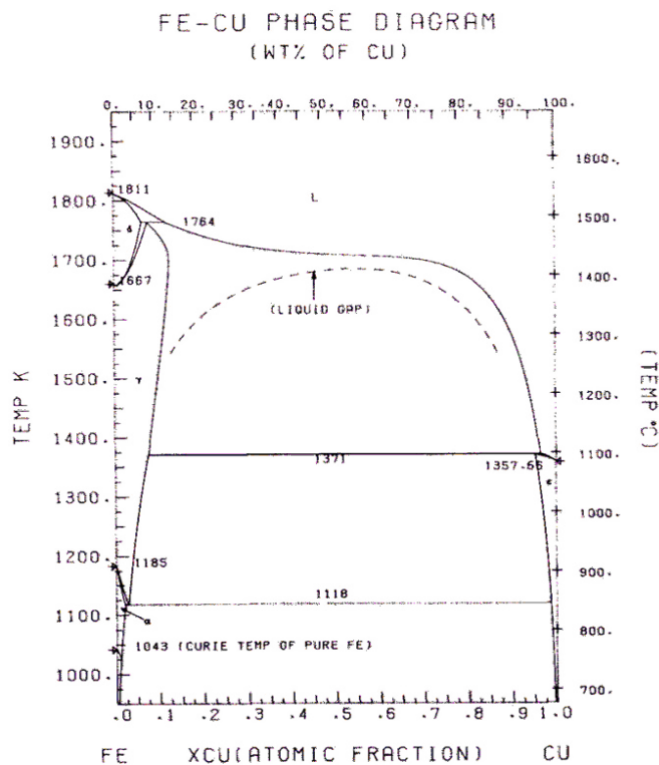


Figure 11: Calculated phase diagram of Fe-Cu [102]

In the twentieth century, JS Benjamin invented the mechanical alloying (MA) method [33], [34], as a dry, high-energy ball milling process to manufacture composite metal powders with a fine, controlled microstructure, originally for high-temperature alloys [34]. Since then, it became a popular approach to alloy metals. The technique produces homogeneous uniform materials by utilizing a repeated process of cold welding, fracturing, and re-welding of the powders using a high energy ball mill [33], [35]–[37]. Figure 12 displays the XRD spectra of the  $Fe_{50}Cu_{50}$  alloy, starting from two separate powders and progressing into the fcc 50-50 mixture that is noticeable after 10 hours of ball milling.

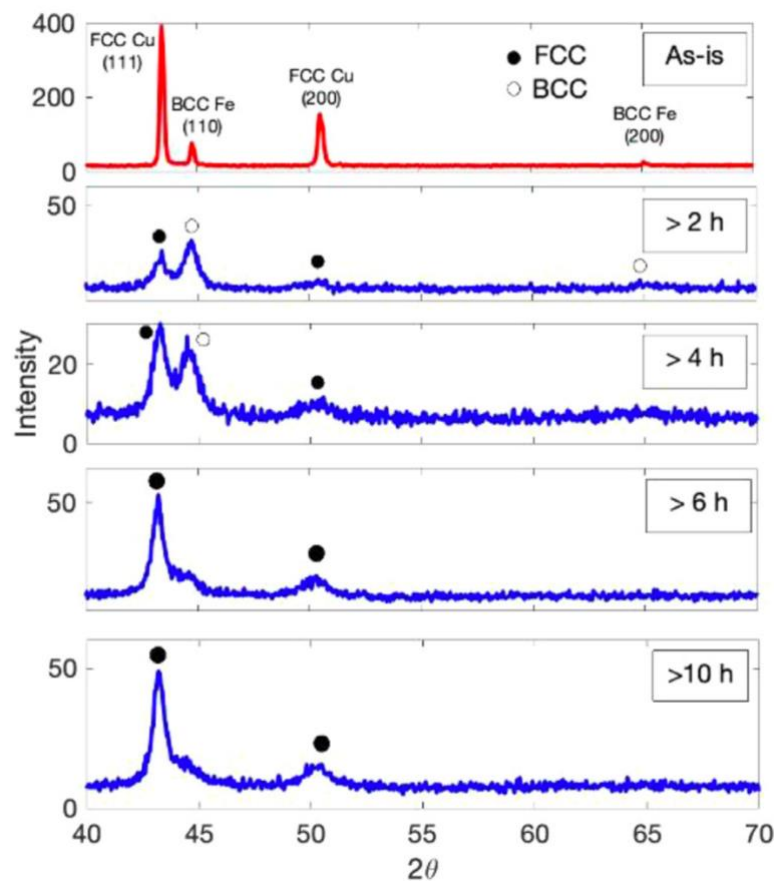


Figure 12: Progressive XRD spectra of milled powder, for  $Fe_{50}Cu_{50}$  [103]

Today, mechanical alloying is often used to manufacture metastable materials [36] such as supersaturated solid solutions [38], intermediate phases [39], quasi-crystalline materials [29], [40], amorphous alloys [41], and high-entropy alloys [42].

## Chapter 3. Methodology

### 3.1. Preparation of $\text{Fe}_x\text{Cu}_{100-x}$

**3.1.1. Materials** High-purity Copper (99.5%) and Iron ( $\geq 99\%$ ) powders purchased from Sigma Aldrich, were used to produce  $\text{Fe}_x\text{Cu}_{100-x}$  alloys, where  $x$  (wt. %) = 25, 35, 50, 65, and 75. Powders were mixed using a Fritsch Pulverisette 7 Premium line planetary ball mill. A 25 mL tungsten carbide grinding bowl and 10mm stainless steel balls were used in the ball milling process for each milling cycle. To prepare the counter-electrode,  $\text{Fe}_{50}\text{Cu}_{50}$  powders were deposited on an Aluminum sheet in a 25mL stainless steel (SS) grinding bowl using a Retsch PM 100 planetary ball mill. Following deposition, the sheet was rolled using in a roller assure to insure a flat surface. The Cryogen-Free Measurement System (CFMS) from Cryogenic Ltd was used to obtain the magnetic and electrical transport properties. Micro Point Pro (MPP)'s iBond 5000 Manual Wedge Bonder, was used to solder the wires onto the compressed  $\text{Fe}_x\text{Cu}_{100-x}$  powders, then placed into the system for the electrical properties measurements. As for the Magnetization, the Vibrating Sample Magnetometer (VSM) set up in the CFMS was used to obtain the required data for the  $\text{Fe}_x\text{Cu}_{100-x}$  powders, and the mass of the powders were measured using Sartorius's Ultra Micro Balance.

**3.1.2. Equipment and Experimental Procedure** For each of the prepared  $\text{Fe}_x\text{Cu}_{100-x}$  alloys, high-purity Copper and Iron powders were weighed according to the composition that is targeted as seen in Table 1. The total mass of the powder in the crucible was 5g of iron and copper powders. Eight 10mm stainless steel (SS) balls were used, which corresponds to 1:6 powder to SS balls mass ratio and placed along with the powders in a 25mL tungsten grinding bowl. Fritsch Pulverisette 7 ball miller was set to milling speed of 600rpm for 10 hours for each of the considered compositions.

Table 1: Iron and Copper Mass measurement for each target composition

Target Composition	Fe Powder (g)	Cu Powder (g)
$\text{Fe}_{25}\text{Cu}_{75}$	1.25	3.75
$\text{Fe}_{35}\text{Cu}_{65}$	1.75	3.25
$\text{Fe}_{50}\text{Cu}_{50}$	2.50	2.50
$\text{Fe}_{65}\text{Cu}_{35}$	3.25	1.75
$\text{Fe}_{75}\text{Cu}_{25}$	3.75	1.25

To understand the chemical composition information, the crystal structure, phase purity, and chemical homogeneity of the studied material were analyzed by Panalytical X'pert3 powder X-ray diffraction (XRD) and further complemented by

energy-dispersive X-ray spectroscopy (EDX, Oxford Instruments), a small sample of each powder was set aside to obtain the results of these tests.

Furthermore, electrical transport properties were measured using Cryogenics Ltd. high field system with vibrating sample magnetometer option in a cryogenic physical property measurement system. To prepare the sample, 0.35g of each powder was compressed into small pellets using a mechanical press as seen Figure 13 and Figure 14.



Figure 13: Mechanical Press

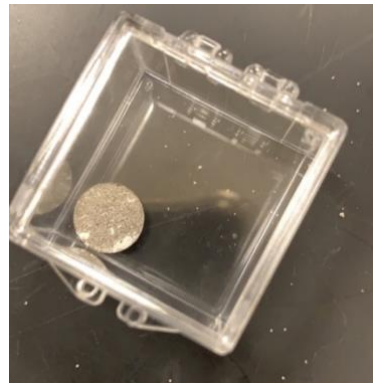


Figure 14:  $Fe_xCu_{100-x}$  Pellets

Using Micro Point Pro (MPP)'s iBond 5000 manual wedge bonder in Figure 15, micro-wires were soldered onto the  $Fe_xCu_{100-x}$  pellets in Figure 16. This is then placed into a chip holder and loaded into the Cryogen-Free Measurement System.



Figure 15: MPP's iBond 5000 Manual Wedge Bonder



Figure 16:  $Fe_xCu_{100-x}$  after soldering wires onto it to load into the Cryogen System

The cryostat was a closed cycle helium cryostat with a variable temperature insert (VTI) in which the VTI and sample temperatures were measured and controlled with a tolerance of 5mK. The Electric transport properties were measured using the 4-



probe method which uses a Keithley 2182A nano voltmeter and Keithley 2461 source measure unit in delta mode for the highest sensitivity. In the 4-probe method a bias current of  $100\mu\text{A}$  used. In the case of the Fe-Cu metal alloy, low resistance is expected as it is a conductor by nature, therefore, the purpose of using a 4-probe, compared to the 2-probe is to eliminate the effect of contact resistance present in the alloy and obtain the most accurate results for this case.

Additionally, magnetization measurements were carried out on pressed powder specimens of known weight. The weight of the powders were obtained using an Ultra Micro Balance to ensure accuracy. The powders were placed into capsules, then sealed off and placed into non-magnetic straws, then placed into the Vibrating Sample Magnetometer set up, the frequency of the function generated is set to match the frequency of the resonance frequency of the material. The set-up is then placed into the Cryogen-Free Measurement System and set to run for an hour at room temperature. With the VMS, the vibration of the material is simulating a change in area to obtain a reading on the magnetic flux.

The Cryogen-Free Measurement System (Figure 17) is a powerful multi-purpose system that was used to obtain the magnetic and electrical transport measurements.

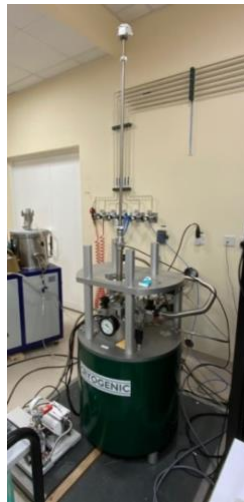


*Figure 17: Cryogen-Free Measurement System*

### **3.2. Counter-electrode preparation**

As the selected replacement of the platinum electrode, the Fe-Cu counter electrode was prepared by depositing  $\text{Fe}_{50}\text{Cu}_{50}$  powder into a  $10.0 \times 2.0 \text{cm}^2$  with 0.2mm thickness aluminum sheet. The aluminum thin sheet was placed in the inner

circumference of a 25mL stainless steel grinding bowl along with 3.7g of  $\text{Fe}_{50}\text{Cu}_{50}$  powder. A Retsch PM 100 planetary ball mill was used to process the Al sheet/powders for 10 hours at 600rpm as seen in Figure 18.



*Figure 18: Deposition of  $\text{Fe}_{50}\text{Cu}_{50}$  on Aluminum Sheet using Retsch PM 100 planetary ball mill*

This process results in the deposition of the iron copper alloy onto the aluminum sheet. During the deposition process, the powder is not consumed completely (only 0.1533g was deposited onto the sheet) but it is important to have sufficient amount of powder to ensure proper deposition onto the aluminum sheet. To ensure the deposition of the powder into the aluminum sheet, the resulting sheet was tested using energy-dispersive X-ray spectroscopy (EDX) to identify the elemental composition of the materials.

Following the deposition, the sheet was rolled using a HK Malvi Wire Sheet Roller (Figure 18) to flatten the aluminum sheet and ensure that the Fe-Cu powder is pressed into the electrode. In addition, this process guarantees no microscopic ridges that may cause an open circuit while testing.



Figure 19: Flattening the Al-FeCu electrode using the HK Malvi Wire Sheet Roller

### 3.3. TiO<sub>2</sub> Photoelectrode

**3.3.1. Materials** The type of transparent and conductive substrate (TCO) used is fluorine-doped tin oxide (FTO) coated glasses. As for the dye, Ruthenizer 535-bisTB was selected. Ready-to-use Iodolyte electrolytes (Z-50) was purchased to be used as an electrolyte in the cell. Drilled platinum (glass) electrodes were selected for the counter-electrode. TiO<sub>2</sub> (anatase) nanocrystalline powder was purchased and used to produce the mesoporous layer. All previously specified materials were procured from Solaronix, Switzerland and were used without further purification. Polyethylene glycol (PEG 600) is used with the anatase powder to produce the mesoporous layer, the item was procured from S D Fine Chem Limited. Testing of the cells was done using Sciencetech Solar Simulator in the American University of Sharjah, Ossila Solar Cell I-V Test System, and RERA Solutions Solar Measurement's Silicon Reference Cell.

**3.3.2. Equipment preparation** Prior to beginning the experimental procedure, the FTO substrates and drilled platinum electrodes were thoroughly cleaned, by sonicating them in Acetone for 15 minutes, followed by ethanol for another 15 minutes, and finally with de-ionized water for a final 15 minutes using an ultrasonication bath (Model 2510, Branson, USA). The substrates were then thoroughly air dried and UV treated with the conductive side facing upwards using Jelight's Model 24 UVO Cleaner® for 20 minutes. Equipment preparation was completed in the University of Sharjah's Center Advanced Materials Research Lab.

**3.3.3. TiO<sub>2</sub> mesoporous layer** TiO<sub>2</sub> paste was prepared with an existing template that was used by Alami et al. [104], where a 1:1 mass ratio of the TiO<sub>2</sub> nanocrystalline powder and PEG 600 were grounded using a pestle and mortar for 30 minutes, resulting in a thick, homogenous paste as seen in Figure 20 and Figure 21.



Figure 20: TiO<sub>2</sub> nanocrystalline powder



Figure 21: Addition of PEG to the TiO<sub>2</sub>

The paste was then deposited on the treated FTO with an active area of 0.25cm<sup>2</sup> (0.5 x 0.5 cm) using doctor blading method. The FTO was then annealed using step-by-step method where the temperature is increased to 450 °C at a rate of 10 °C per minute, then maintained at that temperature for 1 hour as seen in Figure 22. Once peak temperature is reached, the temperature is gradually decreased until it reaches room temperature and is set for dye-loading.



Figure 22: Annealing of TiO<sub>2</sub> at 450°C

The Ruthenium dye was prepared using Ruthenizer 535-bisTB purchased from Solanoix. The dye was prepared by mixing 50ml of Ethanol and 3mg of N719 powder [13]. The TiO<sub>2</sub> covered FTO was soaked in the dye for 24 hours in a dark area, such as the storage cabinet seen in Figure 23 and Figure 24, to ensure the dye loading. Once the

process is complete, the photoelectrodes are removed and the area around the TiO<sub>2</sub> is gently cleaned using ethanol to remove any excess dye-residue.



Figure 23: Overnight Dye-loading in dark area

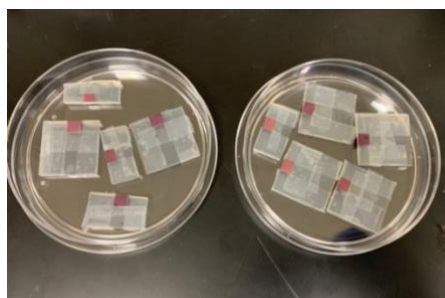


Figure 24: Cells after cleaning and insulating

### 3.4. Dye-Sensitized Solar Cell Assembly and Testing

For the reference cell, the drilled platinum electrodes (counter-electrodes) were then placed on top of the photo-electrode as can be seen in Figure 25. The electrolyte was finally injected into the cell to complete the assembly of the inverted electrochemical cell.

As for the cell with the Fe<sub>50</sub>Cu<sub>50</sub> counter electrode being tested, the Fe<sub>50</sub>Cu<sub>50</sub> coated area is placed on top of the photoelectrode, and the electrolyte is injected between the layers. The schematic provided in Figure 26 displays how the Fe<sub>50</sub>Cu<sub>50</sub> were assembled.



Figure 25: Assembled Dye-Sensitized Cell

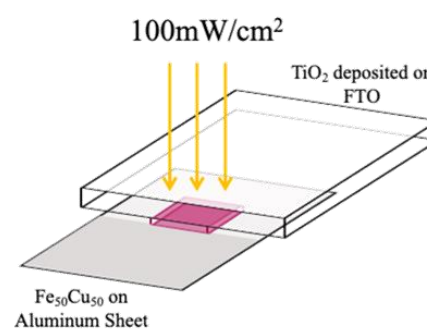
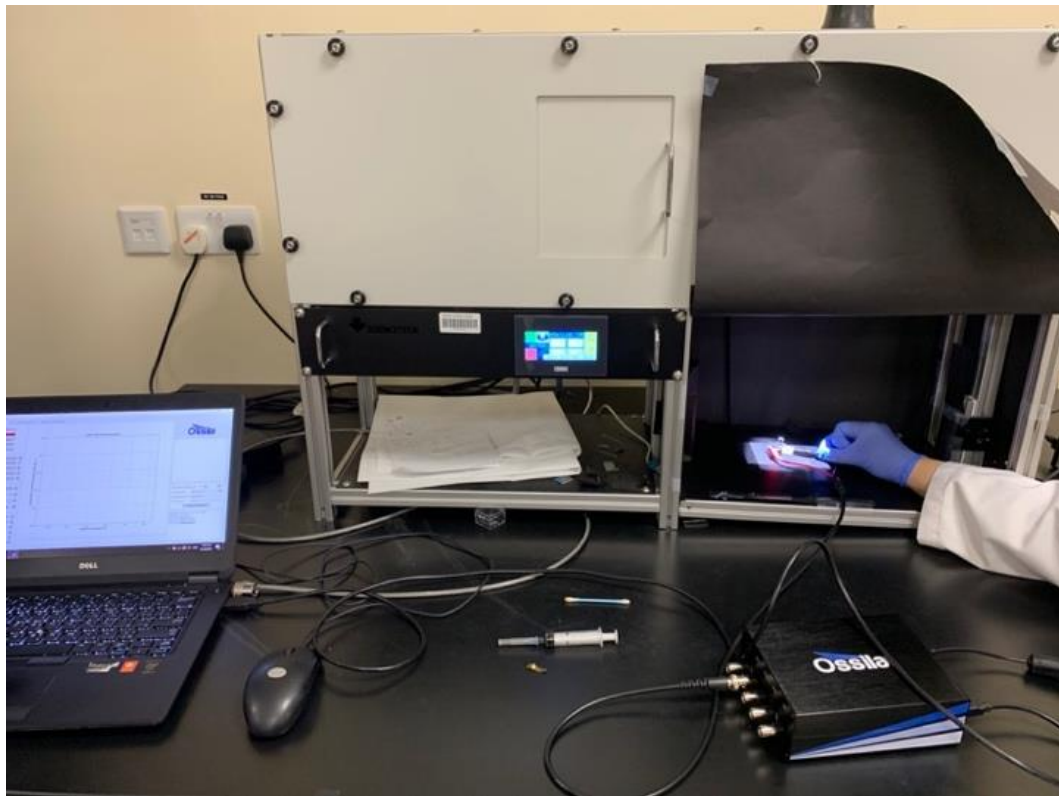


Figure 26: Schematic of the cell using Fe<sub>50</sub>Cu<sub>50</sub>

The cells were tested using the Sciencetech Solar Simulator in the American University of Sharjah and the University of Sharjah's Abet Technologies' SunLite™ Solar Simulator. The setup was connected to Ossila Solar Cell I-V Test System and using Ossila Solar Cell IV program to obtain the I-V curve, efficiency, fill factor, open circuit voltage, short circuit current, and internal resistance. The voltage supplied

throughout the testing process ranged from -0.3V to 0.8V, at an increment of 0.01V, and a voltage rest of 0.7s, as seen in Figure 27. Each cell was first tested using the platinum counter electrode, then the Fe<sub>50</sub>Cu<sub>50</sub> counter electrode, and all cells were tested with the TiO<sub>2</sub> electrode facing down to guarantee the results obtained were with reference to the conventionally used electrode.



*Figure 27: Solar Cell Testing Set-up*

To ensure the consistency and accuracy of the results obtained, different batches were prepared. The cells were tested under the same conditions, following Standard Testing Conditions (STC), i.e. Air Mass 1.5 G condition (A.M 1.5 G condition) where 1 sun is defined as equal to 100mW/cm<sup>2</sup> of irradiance, and at 25°C room temperature following the IEC 60904-3:2008 Standard. To obtain these standards, the sun simulator was first calibrated using RERA Solutions Solar Measurement's Silicon Reference Cell as seen in Figure 28, the fan option in the solar simulator provided the temperature required, and the intensity is modified before each batch-test to ensure that the 100mW/cm<sup>2</sup> is always achieved.



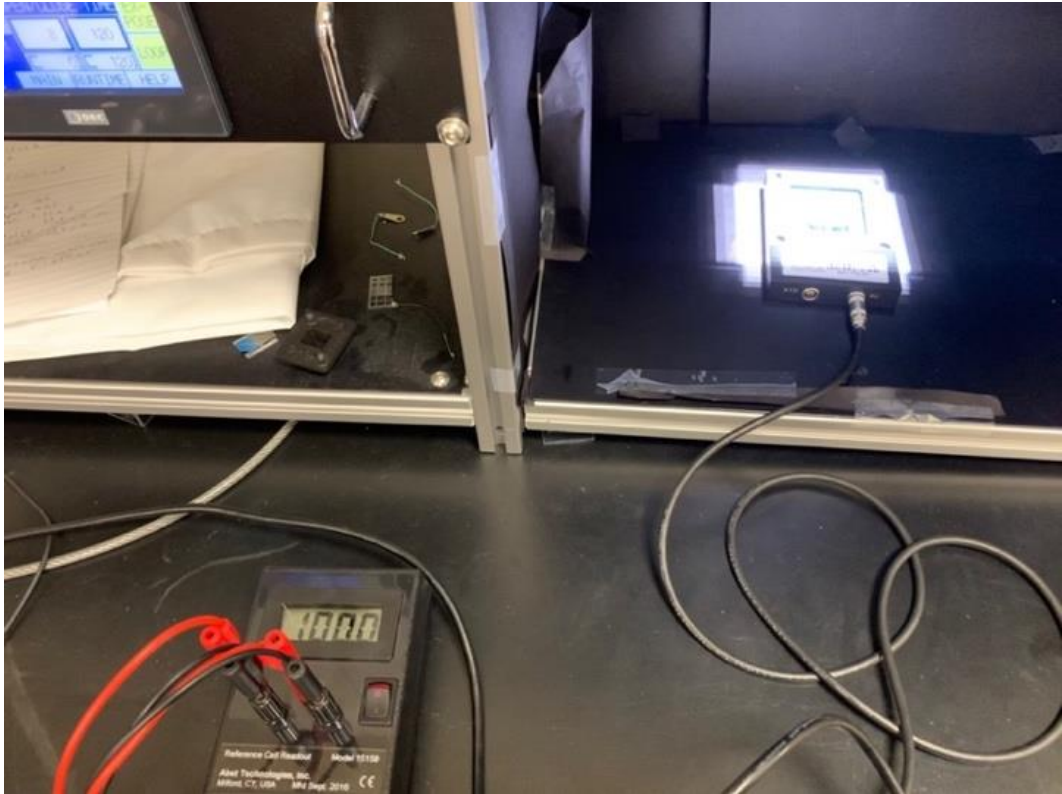


*Figure 28: Calibration of the ScienceTech Solar Simulator using RERA Solutions Reference Cell*

## Chapter 4. Results and Discussion

### 4.1. Scanning Electron Microscope (SEM) and EDX

The scanning electron microscope (SEM) micrograph images were collected at different magnifications for all the  $\text{Fe}_x\text{Cu}_{100-x}$  alloys. A representative SEM image for one of the compositions ( $\text{Fe}_{65}\text{Cu}_{35}$ ) is shown in Figure 29. The resulting particle size averaged around  $100\mu\text{m}$  in diameter for the shown case. However, it should be pointed out that a considerable variation in powder diameter was observed within each batch, and among different batches. The difference between batches is potentially induced by composition differences. For better control of the resulting powder size, the processing condition will need to be optimized (e.g., ball milling time) for each alloy composition. In this work, however, the ball milling process was kept the same for all the considered compositions for the  $\text{Fe}_x\text{Cu}_{100-x}$  alloys where  $x$  (%) =25, 35, 50, 65, and 75. This variation, although not fully explored in this work, is not expected to have a significant impact on the reported measurements.

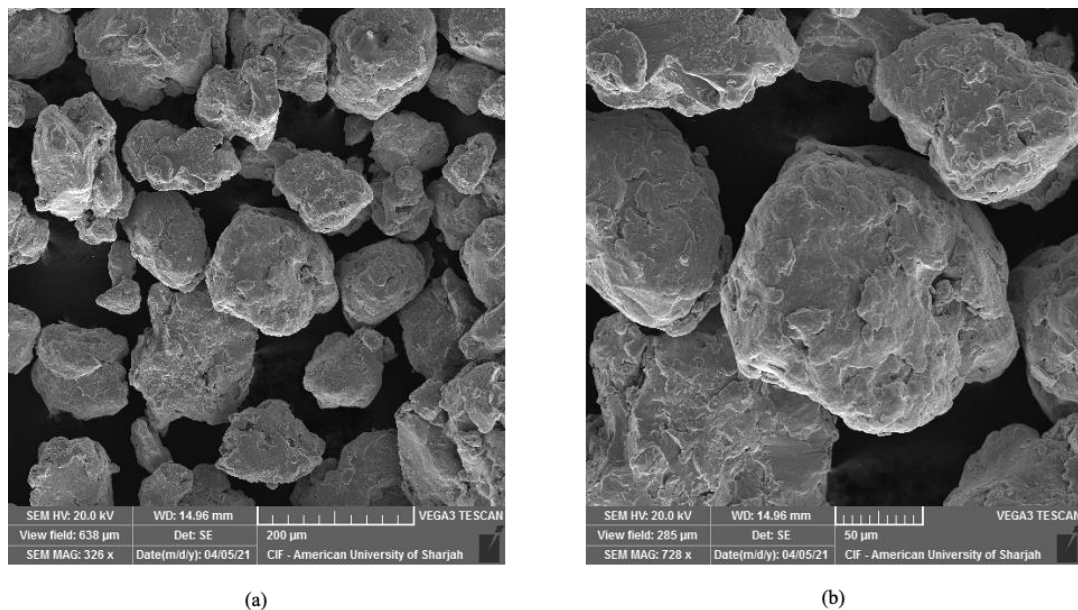


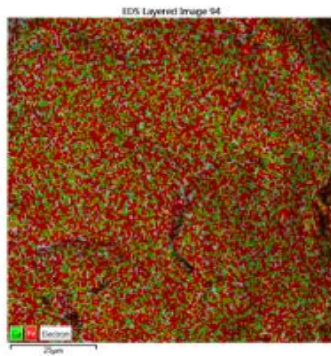
Figure 29: (a) SEM micrograph images for the prepared  $\text{Fe}_{65}\text{Cu}_{35}$  powder. (b) higher magnification image.

### 4.2. Energy Dispersive X-Ray (EDX)

To evaluate the chemical composition of the prepared powders, Energy Dispersive X-Ray (EDX) analysis was conducted for all the  $\text{Fe}_x\text{Cu}_{100-x}$  powders. Figure 30 displays a sample of the results obtained for a single  $\text{Fe}_{65}\text{Cu}_{35}$  particle, where (a) displays EDS layered image of a single  $\text{Fe}_{65}\text{Cu}_{35}$  particle, (b) indicates the Iron composition and



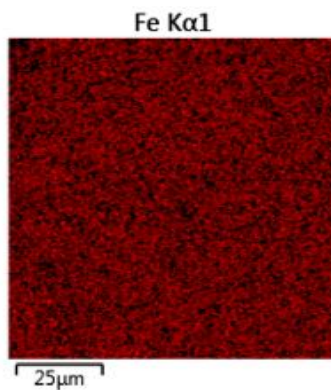
distribution in that particle, and (c) shows the Copper composition and distribution, and measure chemical composition is provided where it presents the exact weight percentage of Iron and Copper in that particle. The resulting chemical composition was very close to the intended alloy (e.g., measured Fe 65.9 wt.% -target Fe 65 wt.%). In addition, the collected elemental maps confirm a uniform distribution of Fe and Cu with no signs of segregation or clustering. This provides confidence in the processing method and that successful alloying was achieved through mechanical ball milling, a method that does not require the addition of heat.



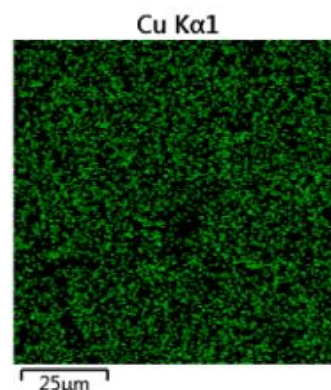
(a)

**Measured Chemical Composition:**

Target Composition	Fe wt%	Cu wt%
$Fe_{65}-Cu_{35}$	65.9	34.1



(b)



(c)

Figure 30: EDX maps of a single  $Fe_{65}Cu_{35}$  particle, (a) displays EDS layered image of a single  $Fe_{65}Cu_{35}$  particle (b) indicates the Iron composition and distribution in that particle, (c) indicates the Copper composition and distribution, and measure chemical composition provides the exact weight percentage of Iron and Copper in a single  $Fe_{65}Cu_{35}$  particle

All the prepared alloys were investigated using EDX. Table 2 presents the compositions obtained from EDX map for each of the synthesized alloys. In all cases, the measured composition matched the target composition, and a uniform distribution of elements was confirmed.

Table 2: Target composition and the EDX results for each  $Fe_xCu_{100-x}$  alloy

Target Composition	Fe wt.%	Cu wt.%
Fe	100	0
Fe <sub>75</sub> -Cu <sub>25</sub>	76.9	23.1
Fe <sub>65</sub> -Cu <sub>35</sub>	65.9	34.1
Fe <sub>50</sub> -Cu <sub>50</sub>	51.4	48.6
Fe <sub>35</sub> -Cu <sub>65</sub>	34.1	65.9
Fe <sub>25</sub> -Cu <sub>75</sub>	27.1	72.9
Cu	0	100

### 4.3. X-Ray Diffraction (XRD)

The XRD patterns for all synthesized alloy powders are shown in Figure 31, including Fe and Cu powders. The XRD pattern of the Fe<sub>75</sub>Cu<sub>25</sub> alloy (Figure 31 (b)) revealed a single-phase bcc structure similar to that of  $\alpha$ -Fe (Figure 31 (a)). On the other hand, alloys with 50%, 35%, and 25% (wt. %) Fe content exhibited a spectrum that belongs to a single-phase fcc crystal structure. The Fe<sub>65</sub>Cu<sub>35</sub> alloy exhibited a dual-phase structure with both bcc and fcc phases. It is observed that the evolution of the structural phases as a function of composition is in line with previous reports on the same topic [103], [105].

As can be noticed, all the mechanically alloyed samples exhibited considerably broader peaks compared to the starting material. Such peak broadening in XRD peaks is often attributed to the crystallite size and local strains in the samples. Considering the fact that the adopted sample preparation technique, which relies on a repeated process of cold welding, fracturing, and re-welding of the powders using a high-energy ball mill [32], [36], [106] leads to a significant mechanical deformation (i.e., plastic strains) in the resulting powders. The resulting increase in defect densities (e.g., dislocations) and induced lattice strains explains such peak broadening in the XRD results.

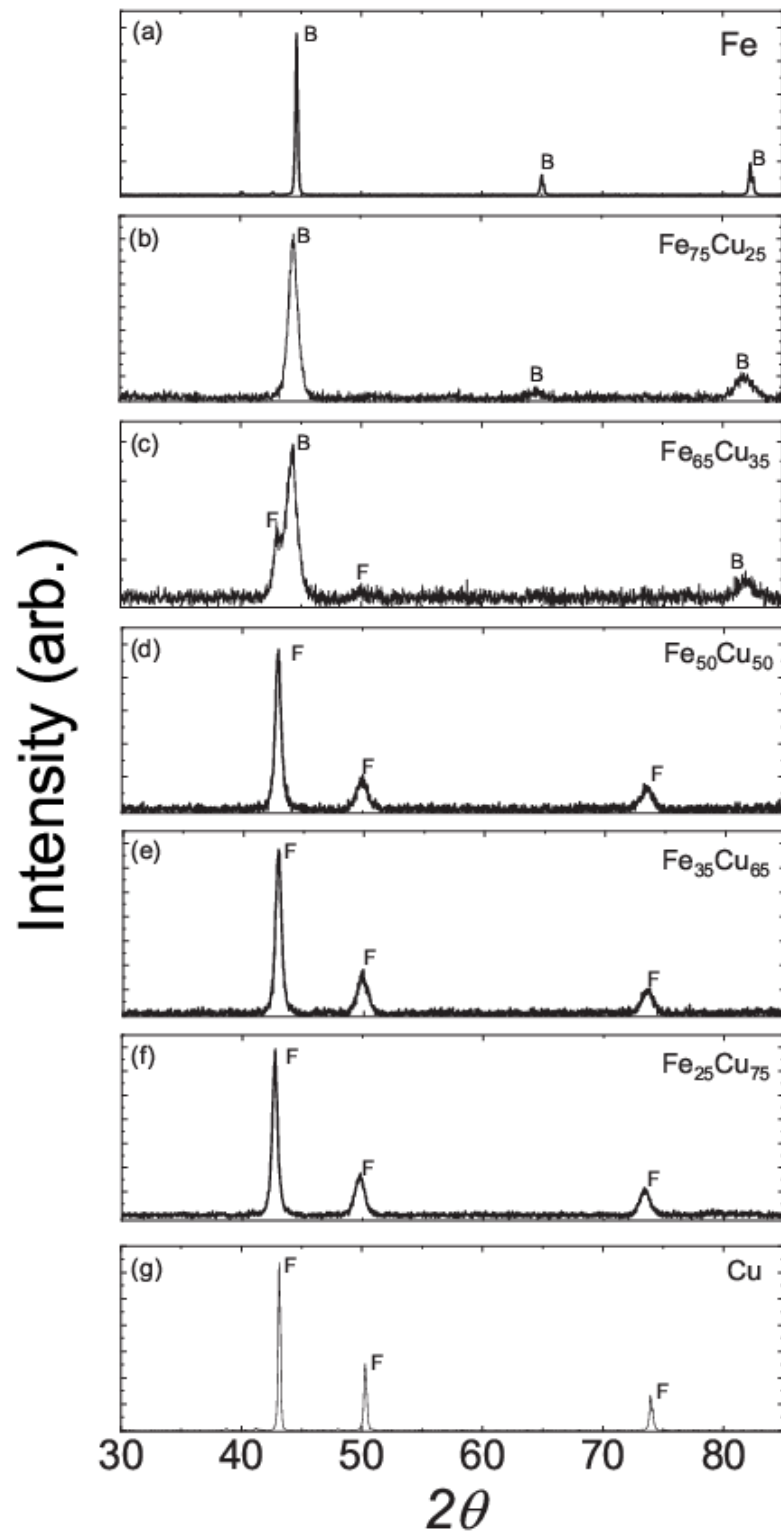


Figure 31 (a)-(g): X-ray diffraction patterns for synthesized  $Fe_xCu_{100-x}$  alloys. Measured spectrums from Fe and Cu starting material are included for ease of comparison. Peaks belong to a bcc phase are marked as B and peaks assigned to the fcc structure are marked

The Lattice parameters were obtained from the XRD data as a function of Fe fraction for all the prepared alloys (see Figure 32). The composition difference along with the variations introduced by the mechanical alloying process (i.e., induced defects

and lattice strains) contribute to the differences in the measured lattice parameters. The associated physical properties, such as electrical and magnetic properties, are also expected to differ for the different alloys. As noted above, studying the physical properties of the Fe-Cu system, and its composition dependencies is one of the objectives of the current work. The following sections provide a comprehensive assessment of the electrical and magnetic properties of the prepared Fe-Cu alloys.

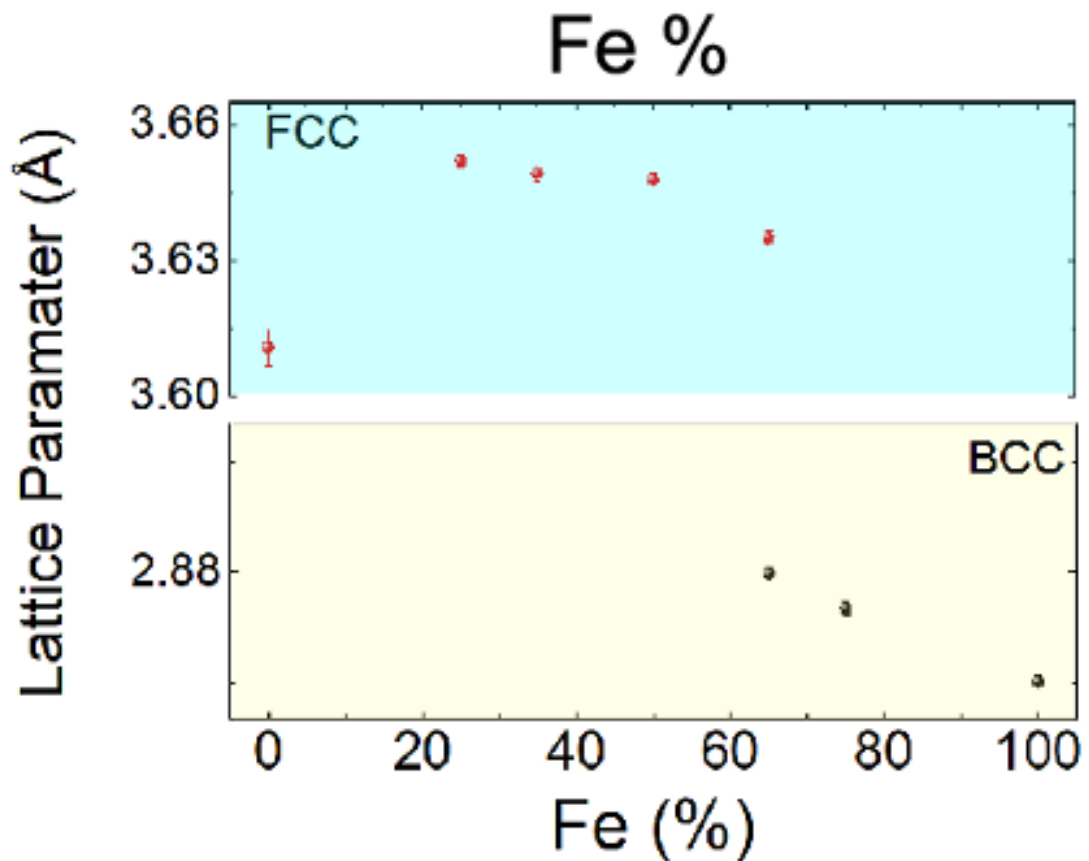


Figure 32: The lattice parameters as a function of Fe fraction in studied  $Fe_xCu_{100-x}$  system

**4.3.1. Electrical Properties** Temperature dependencies of the resistivity of all ball-milled alloys were measured using the 4-probe technique with a bias current value of 100  $\mu$ A and plotted in Figure 33. A microwire bonder was used to attach 25micron Al wires on rectangular-shaped slabs cut from pressed Fe-Cu pellets. Four different samples were considered for each alloy and the results were consistent Residual resistivity values ranging from 34 $\mu\Omega$ .cm to 63 $\mu\Omega$ .cm were measured for our samples. Such values are significantly higher than many binary alloy systems [107].

Indeed, the full-width half-maximums of XRD peaks shown in Figure 31 are very broad which is indicative of large crystallite size distribution and the presence of local stresses and associated defects. The mechanical alloying process by its nature involves high energy collisions hence it is not unusual to have samples with very large residual stresses [108]. In this regard, relatively large residual resistivity values in metallic systems with a significant level of imperfections are expected. All of the studied binary alloys exhibit metallic behavior indicating that the mean free path of the carriers is long enough to avoid the grain boundaries however, their density is large enough to lead large residual resistivity values.

The temperature dependence of the resistivity measurements reveals residual resistivity ratios  $RRR = \frac{R(300K)}{R(2K)}$  between 1.16 and 1.44 for studied alloys. These values are considerably lower than pure metal values however, it is within the reported ranges for binary alloys [107], [109].

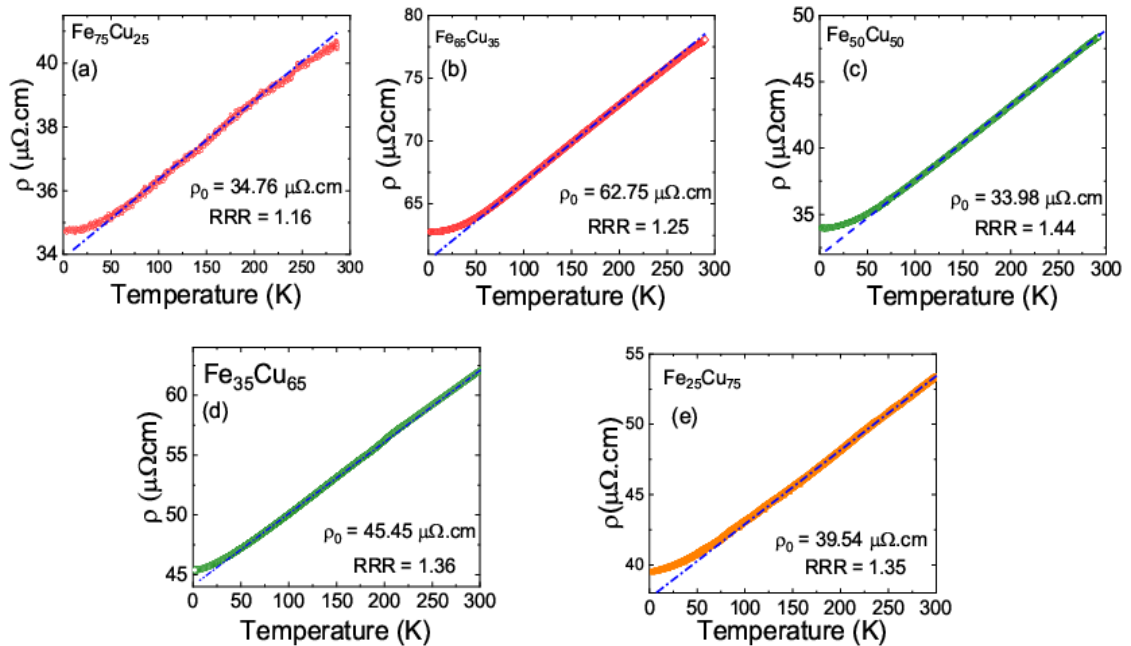


Figure 33 (a)-(e): Temperature dependence of the resistivity for all ball-milled alloys. Residual resistivity ratio (RRR) and residual resistivity ( $\rho_0$ ) are shown for each sample. The linear dashed lines are guides for the eye.

When evaluating the resistivity of a certain alloy, it's important to understand the mechanism of electrical conduction and the dependencies as a function of temperature. Figure 34 displays the temperature dependence of the resistivity of  $\text{Fe}_{25}\text{Cu}_{75}$  system. Where (a) is dedicated to the resistivity measurements for the low

temperature (2-50K) range of the Fe<sub>25</sub>Cu<sub>75</sub> system, and (b) on the other hand, includes readings at high temperature (100-300K) range for the same system. The temperature dependence of the resistivity of Fe<sub>50</sub>Cu<sub>50</sub> system, was also measure in Figure 34–(c) at low temperature (2-50 K) range, and Figure 34–(d) at high temperature (100-300 K) range. The dashed lines displayed in all figures, refer to the line fits.

The mechanism of electrical conduction in these alloys can be studied using power law [110]. This in correlation with the Bloch-Gruneisen theory, where electrical resistivity of the material (whether it is at high or low temperatures) is still temperature dependent. Meaning that the qualitative picture of the power law in case of temperature dependent resistivity is relevant.

In this regards a T<sup>2</sup> dependence (fermi liquid behavior) of the R(T) is a typical feature in metallic systems and is often interpreted to arise from electron-electron scattering events [110], [111]. The samples prepared exhibited typical Fermi–liquid behavior up to temperatures of around 50K. In this temperature range, the temperature dependence of the resistivity can be modeled using  $\rho(T)=\rho_0+\rho_2T^2$  expression down to 50% Fe concentration where  $\rho_0$  is the residual resistivity value and  $\rho_2$  is the resistive constant. A representative example of such fit is given in Figure 34 (a) for Fe<sub>50</sub>Cu<sub>50</sub>.

However, such expression fails to fit the low-temperature dependence of the resistivity for Fe content less than 50%, as indicated by the blue dashed line in Figure 34 (b) for the Fe<sub>25</sub>Cu<sub>75</sub> sample. Interestingly, measured data can be modeled with  $\rho(T)=\rho_0+\rho_{3/2}T^{3/2}$  where  $\rho_{3/2}$  is the resistive constant. T<sup>3/2</sup> resistivity behavior fits perfectly to measured data as revealed in the black dashed line in Figure 34 (c). In this study, the T<sup>3/2</sup> dependence of resistivity explanation relies on the magnon-mediated scattering of electrons in different subbands of the exchange-split conduction band in the presence of weak disorder and scattering of electrons in different subbands with the interaction mediated by helimagnons with and without disorder [112]. The second explanation is only applicable to collinear magnetic structures like helimagnets.

The unusual dependence of the resistivity over-temperature extents to higher temperature ranges in our alloys. T-linear dependence of the resistivity is very visible in all studied alloys, as observed in the straight lines, blue dashed lines in Figure 33 (a)-(e). Such linear dependence is very clear in the 100K-300K range for alloys with higher Cu concentrations. Linear fits using  $\rho(T)=\rho_0+\rho_1T$  expression were performed on the

Fe<sub>25</sub>Cu<sub>75</sub> and Fe<sub>50</sub>Cu<sub>50</sub> samples as seen in Figure 34 (b) and (d). In this expression  $\rho_0$  is residual resistivity whereas,  $\rho_1$  is a resistive constant. T-linear dependence of resistivity most commonly known as “*strange metallicity*” has been one of the most challenging problems during the last 30 years in the context that its origin suggested being related to the high-temperature superconductivity in strongly correlated electron systems [113]. Strange metallicity is characterized by a linear-T resistivity and relatively high metallic resistivity at room temperatures (larger than 10 $\mu\Omega$ .cm) [114]–[116]. In high-temperature superconductors (cuprates, or copper oxides that present superconducting properties at high-temperatures [117]), strange metallicity is explained through strong electron correlation or electron interaction or quantum criticality effects [112], [113], [116].

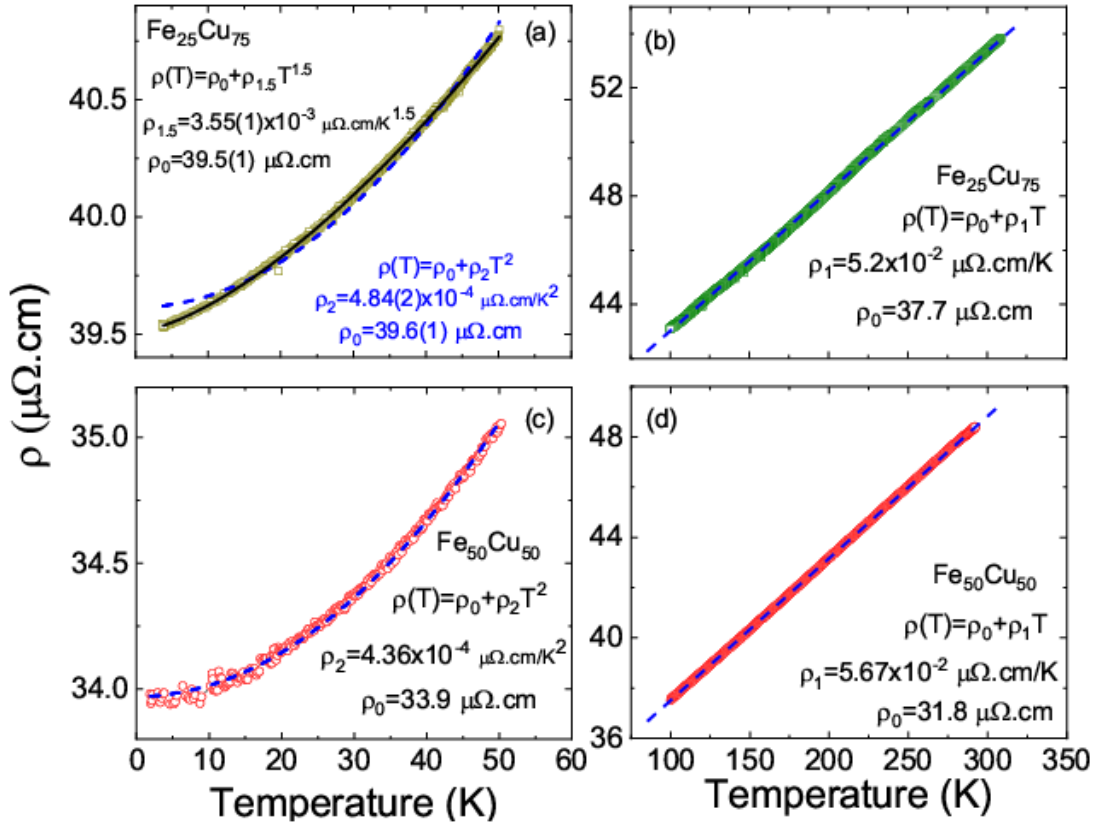


Figure 34 (a)-(d): Temperature dependence of the resistivity of Fe<sub>25</sub>Cu<sub>75</sub> and Fe<sub>50</sub>Cu<sub>50</sub> alloys

**4.3.2. Magnetization Properties** Following the analysis of the magnetization, all the mechanically alloyed Fe-Cu were ferromagnetic in the measurement range of 2-350K. The temperature dependencies of magnetization of all samples were plotted (including the starting Fe powder) as observed in Figure 35 (a).

As can be noticed, the magnetization measured in a field of 0.5T at 2K dropped monotonically from 195 emu/g to 55 emu/g from elemental starting powder Fe to Fe<sub>25</sub>Cu<sub>75</sub> alloy.

For the convenience of comparison, the temperature dependence of the magnetization-to-magnetization value was normalized at 2K (Figure 35 (b)). It was noticed that the Curie temperatures ( $T_c$ ) of the alloys with more than 35% Fe content were higher than the measurement limits of our experimental setup. Therefore, the only measurable  $T_c$  was observed in Fe<sub>25</sub>Cu<sub>75</sub> and determined to be 250K. A Curie temperature of 350-500K has been reported for Fe<sub>x</sub>Cu<sub>100-x</sub> for compositions higher than 35% Fe content [26][92]. The results obtained were consistent with these reported values, as can be noticed in in Figure 35 (b), the percentage drops revealed compared to 2K magnetization indicate magnetic transition temperatures in the range of 350-500K.

The saturation magnetic moments were calculated at 2K for all samples. As indicated in Figure 35 (c), where the magnetic moments monotonically decreased from 2.28  $\mu_B$ /Fe for starting Fe powder to 0.51  $\mu_B$ /Fe in Fe<sub>25</sub>Cu<sub>75</sub> specimen. The reported magnetic moments observed are in line with previously reported values [26] [92] [30]. The origin of the magnetism in the Fe<sub>x</sub>Cu<sub>100-x</sub> system has been the subject of very few studies as the experimental realization of single-phase Fe<sub>x</sub>Cu<sub>100-x</sub> specimens is very difficult [92], [118].

Fe-based alloys are very susceptible to the subtle variations in the atomic volume or interatomic Fe-Fe distance [97]. Specifically, any alteration on the  $3d$  band of the Fe (whether it is change in the interatomic distances, change in the local symmetry, or alteration of nearest-neighbor interactions) will increase the density of states near the Fermi level and therefore an enhancement of the ferromagnetic interactions. In previously investigated invar alloys, the magnetism is described a result of a transition from a low spin, low volume to a high spin, high volume state [98], [119]. On the other hand, in the investigated Fe-Cu system, based on the lattice parameters determined from the XRD (see Figure 32), the volume per atom corresponds to a value of 12.13Å<sup>3</sup> for Fe<sub>50</sub>Cu<sub>50</sub> while it is 12.17Å<sup>3</sup> for Fe<sub>25</sub>Cu<sub>75</sub>. All the estimated volumes for the alloy system obtained suggest a high volume state consistent with Weiss model predictions of ferromagnetic ground state [120].



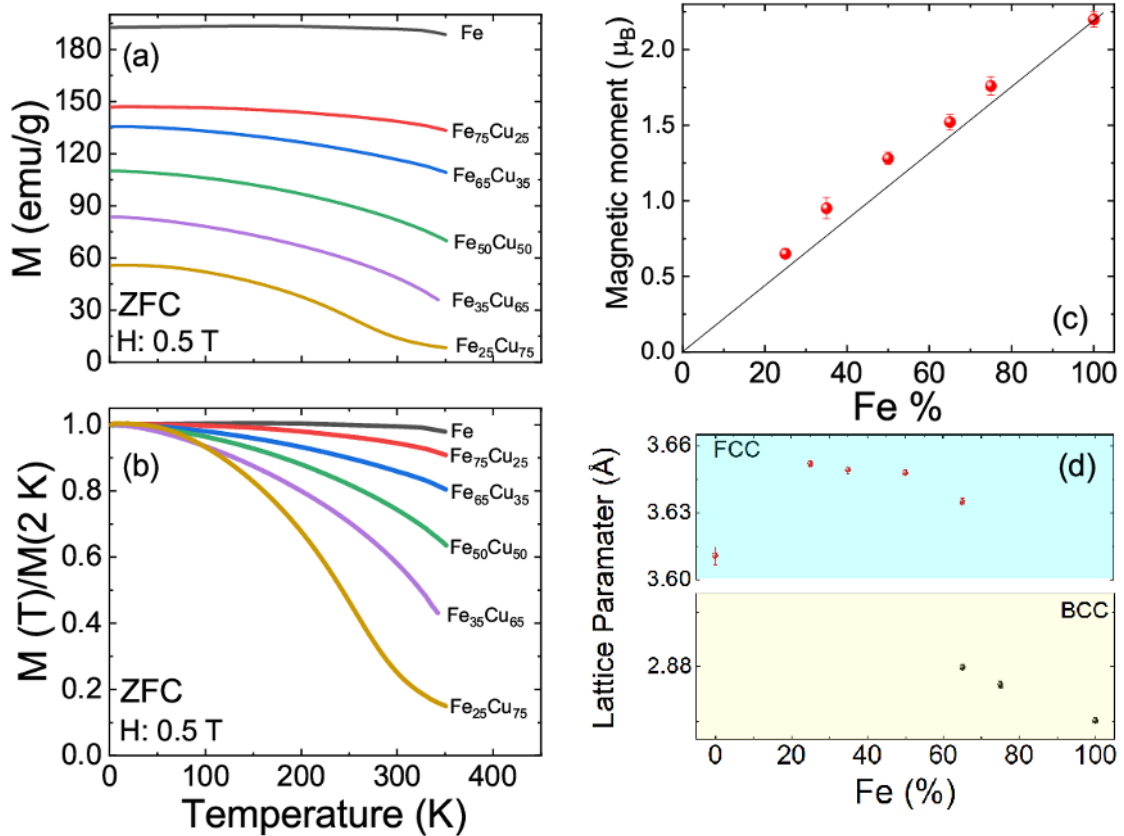


Figure 35: (a) Temperature dependence of the zero-field cooled (ZFC) mass magnetization for all mechanically alloyed specimens. The magnetization data for Fe starting powder has been also presented for comparison. (b) Temperature dependence of the magnet, (d) The lattice parameters as a function of Fe fraction in studied  $Fe_xCu_{100-x}$  system

**4.3.3. Magnetoresistance** The magnetic field dependence of the resistivity (magnetoresistance) for all mechanically alloyed samples were measured, as seen in Figure 36. The Fe<sub>75</sub>Cu<sub>25</sub> alloy powder did not exhibit very small magnetoresistance (less than 0.02%) within the applied magnetic field ranges up to 5T. On the other hand, in the samples with 65% and 50% Fe content, a small (0.30.5%) negative magnetoresistance was present. Additionally, the 35% and 25% Fe content samples exhibited significantly large negative magnetoresistance as seen in Figure 36.

Negative magnetoresistance can appear when the carrier density increases with the application of a magnetic field [121]–[123]. Observation of negative magnetoresistance in magnetic alloys is very common and explained through the increase of the effective field acting on the localized spins and subsequent suppression of the fluctuation of spins in space and time due to external magnetic fields. Such suppression of spin fluctuations leads to the decrease of resistivity [124].

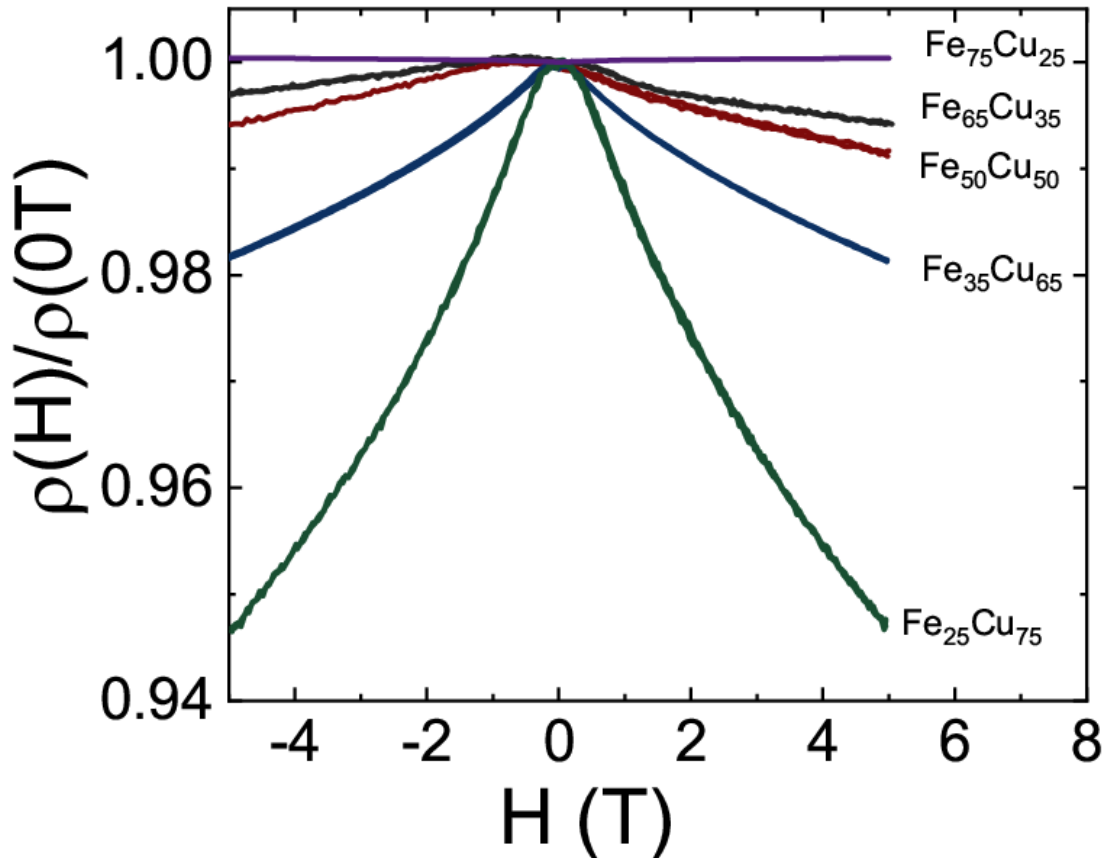


Figure 36: Magnetic field dependence of the resistivity for mechanically alloyed  $Fe_xCu_{100-x}$

#### 4.4. Counter Electrode Analysis

In order to utilize the properties of the  $Fe_{50}Cu_{50}$  alloy powder (a low resistivity of  $49\mu\Omega\text{ cm}$  at  $T\approx 296\text{K}$  as seen in Figure 34 (d)), the MA powders were deposited on the surface of an aluminum sheet using mechanical alloying process. After depositing the Fe-Cu onto the aluminum sheet, it was then rolled to complete the process of producing the counter-electrodes. The rolling of the aluminum sheet ensured that the Fe-Cu is embedded into the aluminum as seen in Figure 37 (at four different magnification), eliminating any chances of an open circuit during the testing process. The Fe-Cu particles are evenly distributed across the surface of the Al sheet, as shown in Figure 37 (a) & (b). Additionally, from Figure 37 (c) & (d) it can be observed how the Fe-Cu is embedded into the aluminum sheet.

To confirm the composition and distribution of the Fe-Cu particles, EDX were conducted on the surface of the Al/Fe-Cu strip. The results of the conducted analysis are presented in Figure 38. The composition of the FeCu is near 50-50 weight ratio, indicating that the process of rolling has not disturbed the originally deposited powder alloy of  $Fe_{50}Cu_{50}$ . It should be noted that the milling process to deposit the Fe-Cu

particles on the Al sheet does not provide a complete and defect free film. This explains the detection of Al in the result reported in Figure 38. In addition, and as observed from the SEM images in Figure 37, some regions have limited deposition with the Al substrate exposed. An example of this is shown in Figure 39. The full extent of the effect of such deposition defects has not been explored in the current work and requires further investigation.

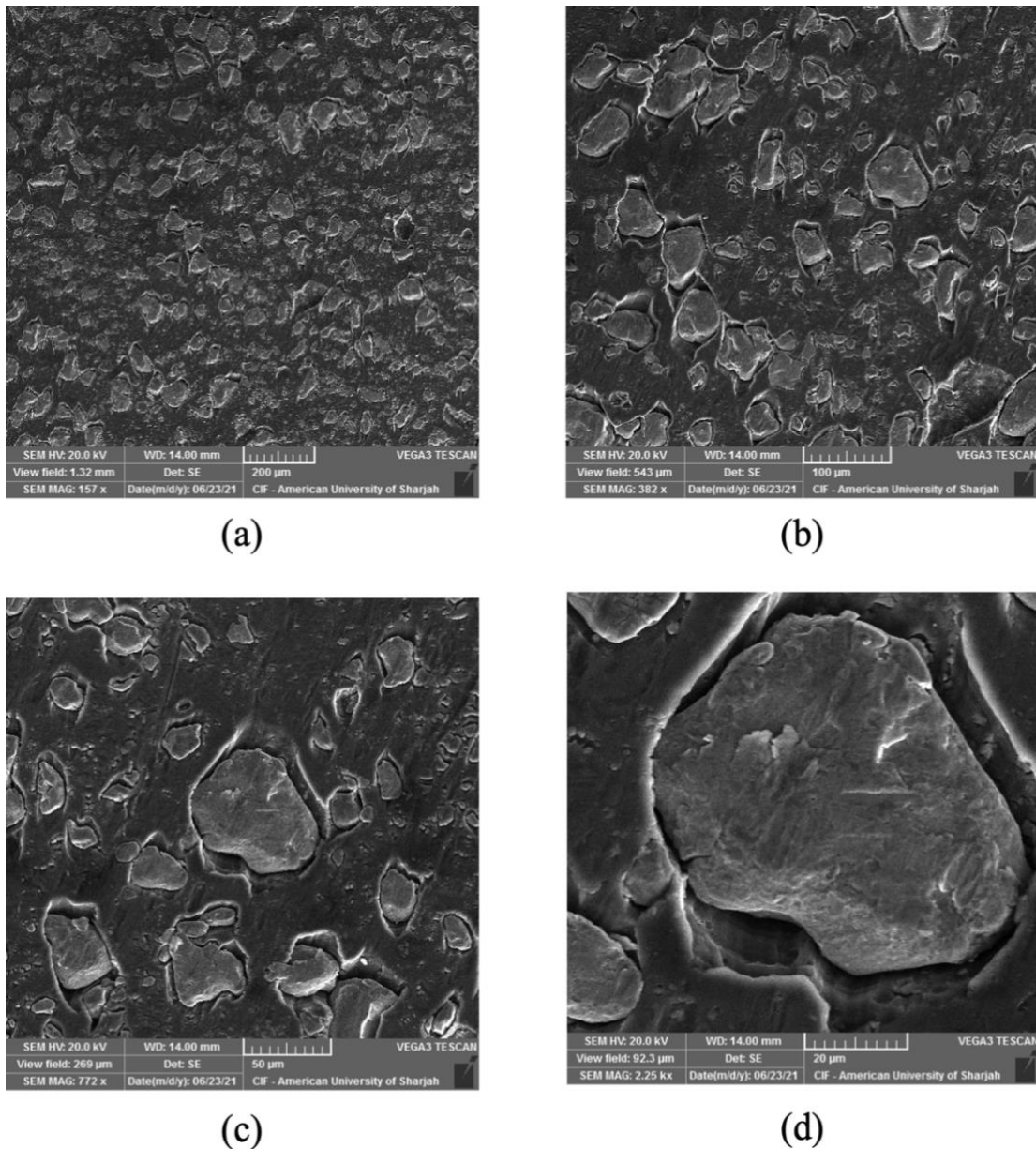
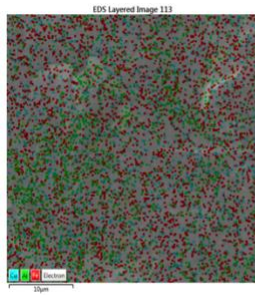
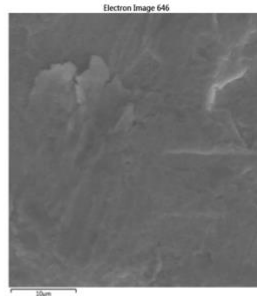


Figure 37: SEM of Rolled Al-Fe<sub>50</sub>Cu<sub>50</sub> Sheet used as counter electrode at different magnifications (a) at view field of 1.32mm, (b) at view field of 543μm, (c) 269 μm, and (d) 92.3μm view field



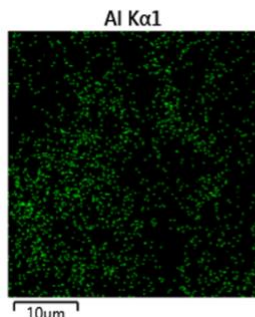
(a)



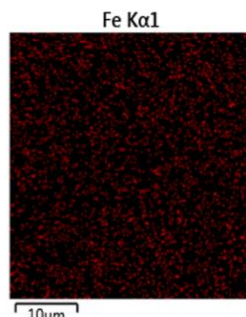
(b)

**Measured Chemical Composition:**

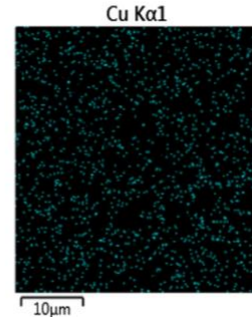
Target Composition	Fe (wt%)	Cu (wt%)	Al (wt%)
Rolled Al-Fe <sub>50</sub> Cu <sub>50</sub>	43.8	36.4	19.8



(c)

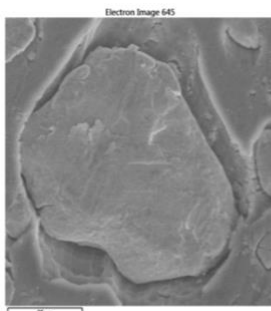


(d)

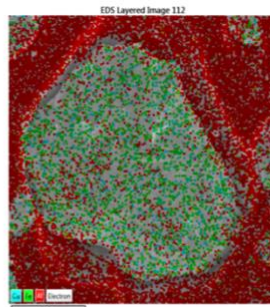


(e)

Figure 38 (a)-(e): EDX maps of a single Fe<sub>50</sub>Cu<sub>50</sub> particle embedded into the Aluminum sheet



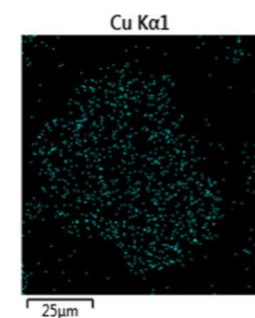
(a)



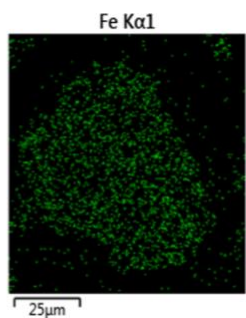
(b)

**Measured Chemical Composition:**

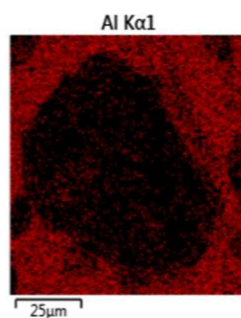
Target Composition	Fe (wt%)	Cu (wt%)	Al (wt%)
Rolled Al-Fe <sub>50</sub> Cu <sub>50</sub>	19.5	17.1	63.4



(c)



(d)



(e)

Figure 39: EDX maps of an Fe<sub>50</sub>Cu<sub>50</sub> particle embedded into the Aluminum sheet, (a) is an electron image, (b) is the EDS layer image of the particle and its surroundings, (c) is the copper concentration and distribution, (d) indicates iron concentration and distribution, (e) indicates the aluminum concentration and distribution surrounding the particle

#### 4.5. Cell Testing

Following the deposition of the Fe<sub>50</sub>Cu<sub>50</sub> powder onto the Aluminum sheet, different cells were constructed and tested. These cells had a platinum counter electrode and Fe<sub>50</sub>Cu<sub>50</sub> counter electrode. Two different batches of cells were produced; first batch (FB): Cells 01 to 04 and a second batch (SB): Cells 05 to 08. The considered number of cells (a total of 8 in 2 different batches) aims to ensure the statistical significance of the results. Table 3, presents a summary of the results obtained from the control cells (i.e., platinum counter electrode). It is evident that the cells had consistent results while operating with the conventionally used platinum electrode (baseline) for the two produced batches (first batch (FB): Cells 01 to 04, second batch (SB): Cells 05 to 08).

Since *Doctor Blading* method was used to deposit the TiO<sub>2</sub> onto the FTO, variation in the results obtained from the cells within each batch is expected. The doctor blading method is a common tape casting method used to produce thin-films [125]. This method can be considered a manual approach, and depending on the blading technique, variation in results can be significant.

Open-circuit voltage is the voltage obtained when the current flowing through the system is equal to zero [126]. The open-circuit voltages obtained with platinum electrodes are above (0.65V), which are considered acceptable voltages, since the cell testing was conducted between -0.3V and 0.8V.

On the other hand, the short-circuit current is the current obtained when near-zero resistance is applied on the cell. In other words, the maximum theoretical current is obtained when zero voltage is applied [127]. The short circuit current and the irradiance perceived by the cell have a linear relationship [128], [129]. Since all cell-testing was conducted under the same conditions, the short circuit current fluctuations observed using this counter-electrode are minimal. These minimal fluctuations observed can be attributed to the thickness of the TiO<sub>2</sub> cells which limits the irradiance perceived from sun simulator. The TiO<sub>2</sub> thickness varies from one cell to the other, as indicated previously due to the deposition method.

These two factors, along with the maximum power obtained, determine the cell's performance. The obtained results (Table 3) showcase this variation for FB and SB which ranges from 2.26% to 3.73%. Since the obtained cells present relatively good performance and consistent values, the baseline obtained can be deemed reliable.



Table 3: Dye-Sensitized Solar Cell Testing Results using Platinum as a Counter Electrode

Platinum Counter Electrode					
Cell Label	Efficiency (%)	FF (%)	V <sub>oc</sub> (V)	I <sub>sc</sub> (mA)	P <sub>max</sub> (mW)
Cell 01	2.4747	59.755	0.65297	6.342	0.61867
Cell 02	2.7789	57.6438	0.66866	7.2097	0.69473
Cell 03	2.7456	73.2264	0.72310	5.1854	0.68639
Cell 04	2.26731	56.3138	0.64988	6.19531	0.56683
Cell 05	2.91286	62.1587	0.71059	6.59479	0.72821
Cell 06	2.50073	52.821	0.68297	6.93207	0.62518
Cell 07	2.86859	58.6598	0.66620	7.34049	0.71715
Cell 08	3.73252	64.7129	0.68768	8.3873	0.94293

When testing the FB using Al-Fe<sub>50</sub>Cu<sub>50</sub> counter electrodes, (also labeled as Cell 01 to Cell 04 in Table 4), the obtained efficiencies are almost zero. These cells were prepared without rolling the Al-Fe<sub>50</sub>Cu<sub>50</sub> sheet. Following the rolling process, which helped remove any surface irregularities and resulted in a relatively flat surface, the obtained efficiencies improved as reported in Table 4 for Cells 05-08.

A noticeable drop in performance can be observed between the platinum and rolled Al-FeCu electrodes. The open-circuit voltage's value is dependent on the operating temperature of the cell. The increase in the temperature results in a higher resistive power loss ( $I^2R$ ) [130]. This can also be observed in Figure 40, where IV curve of the Al-Fe<sub>50</sub>Cu<sub>50</sub> cell is linear, indicating that the resistivity of the material is high. As discussed previously, it was observed that the Fe-Cu resistivity is linear T-dependent. Since the cells are operating at room temperature, this trend and the high metallic resistivity at room temperatures is expected (Figure 34). Due to the fact that these trends occurred after MA, it could be due to the broadening in the XRD peaks observed in Figure 31. A possible solution to this broadening would be heat-treatment of the Fe-Cu powders.

The short-circuit current trends display a similar drop in the obtained results. Since this is a photo-electrochemical device, the ionic transfer plays a crucial role in the redox reaction. Therefore, a presence of a gap between both electrodes, can results in low ionic transfer and thereby lower current. Although rolling of the Al-Fe<sub>50</sub>Cu<sub>50</sub> has

been shown to resolve that issue, as seen between the results of FB and SB in Table 4, the reduced thickness in the Al-FeCu leads to the creation of kinks in the surface of the material during handling and testing. These dents created a gap between both surfaces which possibly resulted in the current drop. A possible solution for this issue would be hammering the sheet instead of rolling it, or the usage of a thicker aluminum sheet that would not significantly lose its structure when rolled or hammered.

Table 4: Dye-Sensitized Solar Cell Testing Results using Fe<sub>50</sub>Cu<sub>50</sub> deposited onto an Aluminum sheet as a Counter Electrode

	Fe <sub>50</sub> Cu <sub>50</sub> Counter Electrode					Comments
	Efficiency (%)	FF (%)	V <sub>oc</sub> (V)	I <sub>sc</sub> (mA)	P <sub>max</sub> (mW)	
Cell 01	0	0	0	0	0	Al-FeCu is not rolled
Cell 02	0	0	0	0	0	
Cell 03	0.002867	12.1041	0.35258	0.06718	0.00072	
Cell 04	0.006808	16.2870	0.30985	0.13490	0.00170	
Cell 05	0.128910	28.5289	0.27563	1.63933	0.03223	Al-FeCu is rolled
Cell 06	0.118345	29.5617	1.27914	0.31297	0.02959	
Cell 07	0.141001	17.8913	0.31717	2.48473	0.03530	
Cell 08	0.262827	22.5602	0.34072	3.41923	0.06571	

Although there is a noticeable enhancement when comparing the platinum counter electrodes (the reference cells) and the rolled Al-Fe<sub>50</sub>Cu<sub>50</sub> counter electrodes, the cell performance remains significantly lower than the platinum electrode cell. This is clear from the current-voltage curve of Cell 05 in Figure 40, which corresponds to values reported in Table 3 and Table 4. As can be seen from Figure 40, the platinum electrode graph (shown in orange) follows a good square shape indicating a high-fill factor (as provided in Table 3, Cell 05, FF (%) = 62.16%). This is a good indicator that the cell being tested is a reliable cell.

Similarly, the power-voltage curve of Cell 05 seen Figure 41 portrays the gap in the power production from both cells, which once again is in line with the results reported earlier. The power curve displays the maximum power for both electrodes, P<sub>max</sub> obtained using the platinum electrode is 0.72821mW, and 0.03223mW using Al-Fe<sub>50</sub>Cu<sub>50</sub>.

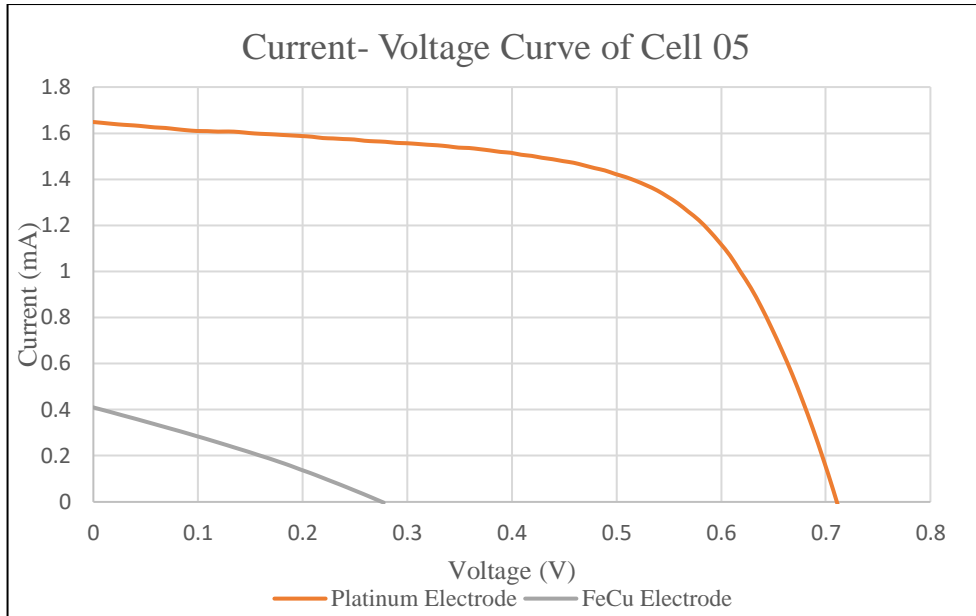


Figure 40: Current-Voltage Curve of Cell 05

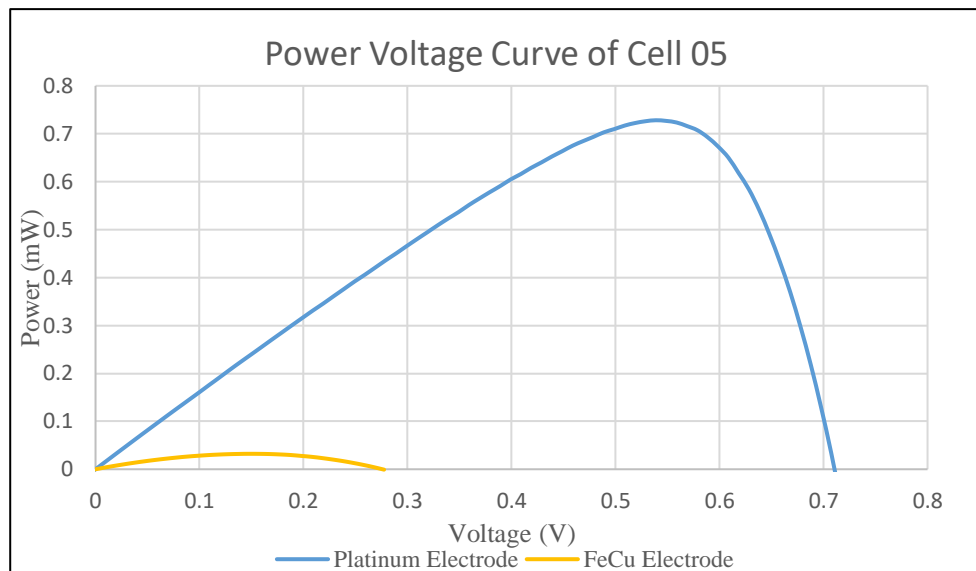


Figure 41: Power-Voltage Curve of Cell 05

#### 4.6. Motivation for the use of Fe-Cu

An economic analysis of the materials and processes used can highlight the contribution of the current work. Platinum electrodes use screen printing process that results in 6-8 $\mu$ m thickness using double print platinum screen printing process [131]. Each platinum electrode used during testing had 20x20mm<sup>2</sup> active area (as specified by the supplier) and is sold for 15AED/piece [132]. Since platinum is highly dense element (density of 21.45 g.cm<sup>-3</sup>), the total mass present in the electrode is estimated to be 32mg of platinum per electrode.



On the other hand, 0.1533g of Fe<sub>50</sub>Cu<sub>50</sub> were used for the deposition onto the 10.0×2.0cm<sup>2</sup> aluminum sheet (as detailed in section 0). To compare both electrodes properly, the mass of the Al-Fe<sub>50</sub>Cu<sub>50</sub> for an area of 20x20mm<sup>2</sup> is approximated as Fe<sub>50</sub>Cu<sub>50</sub> 0.03066g (Fe 0.01533g, Cu 0.01533g).

With this approximation, the distribution across the Al sheet is assumed uniform. For the specifications mentioned, and knowing that the cost of Iron and Copper is 0.220776AED/g and 4.3856AED/g respectively [133], [134], the cost of the Iron Copper used for an active area of 20x20mm<sup>2</sup> is approximately 0.07 AED. Additionally, the aluminum sheet is assumed here is approximated 0.85mm (before rolling), with an area of 4x8ft<sup>2</sup> at the cost of 128 AED/sheet [135], therefore, for the same specifications, the cost of the aluminum sheet with an area of 20x20mm<sup>2</sup> is approximately 0.017 AED. Resulting in the total cost of a single electrode to be **0.09 AED**, compared to the platinum electrode retailed at 15AED.

Understanding the cost of these electrodes and the resulting efficiency is crucial. Since the platinum electrode is an expensive electrode, it is expected to yield significant results. Although it may seem that way at first, but when we compare the percentage per AED, we can understand whether the value invested is actually providing us with desired results.

Therefore, the obtained efficiencies for both electrode types (i.e., platinum and the Al-Fe<sub>50</sub>Cu<sub>50</sub>), were normalized by the corresponding cell cost (Table 5). As can be noticed, the Efficiency-Cost analysis of Cell 08 indicate that although the platinum electrode yields better results, the Al-Fe<sub>50</sub>Cu<sub>50</sub> is good competitor in enhancing the cell's performance. Additionally, seeing as the Al-Fe<sub>50</sub>Cu<sub>50</sub> electrode is almost 12 times cheaper in price compared to the Pt-electrode. The conducted analysis highlights the potential for using Al-Fe<sub>50</sub>Cu<sub>50</sub> as a replacement for platinum. However, significant improvements and further optimization are still required to enhance the resulting efficiency.

Table 5: Efficiency–Cost analysis of Cell 08

Electrode	Efficiency (%)	Cost (AED)	% per AED
Platinum	3.73252068	15	0.24883
Al-Fe <sub>50</sub> Cu <sub>50</sub>	0.262826842	0.09	2.98476

## Chapter 5. Conclusion

To summarize, the exponential increase in global population has been a worrying issue in the energy sector since it translates to an increase in demand. Existing natural resources are continuously depleting and the environmental impact of conventional energy sources is near catastrophic. These aspects have been a great motivator in the energy sector to identify new methods for producing clean and sustainable energy while minimizing any harmful side effects. Since the semiconductor revolution entered the solar energy market, photovoltaic cells have been dubbed a “space age marvel” [136]. Direct conversion of sunlight-to-energy, in a sunlight abundant location such as the United Arab Emirates is logical option. Additionally, since dye-sensitized solar cells, or Grätzel cells, operate on the idea of “low-cost high efficiency cells” they present an attractive candidate in this situation.

The aim of this work was to propose a candidate electrode or counter electrode material. This has been achieved through the selection of the  $\text{Fe}_x\text{Cu}_{100-x}$  system. The counter electrode was produced by synthesizing the  $\text{Fe}_x\text{Cu}_{100-x}$  alloy powders using the mechanical alloying method. The XRD, SEM, and EDX of the powders were analyzed and discussed. Due to the fact that the alloying process technique involves significant mechanical deformation, peak broadening was detected in the XRD of the  $\text{Fe}_x\text{Cu}_{100-x}$  system compared to the starting materials. Moreover, detailed microstructural characterization revealed single phase fcc solid solutions for  $25 \leq x \leq 65$ , single-phase bcc solid solutions for  $75 \leq x < 100$ , and dual-phase (fcc+bcc) alloy in the range of  $x=65-75$ . The EDX analysis confirmed that the weight percentages found in the alloys correspond to the target composition. The composition was also homogeneous with no signs of element segregation or clustering.

Additionally, the electric and magnetic properties were investigated. In the low-temperature range (2-50K),  $\text{Fe}_{50}\text{Cu}_{50}$  alloy exhibited  $T^2$  dependence of the resistivity as expected from typical metals. On the other hand, at low temperatures,  $\text{Fe}_{25}\text{Cu}_{75}$  alloy exhibited  $T^{3/2}$  dependence of the resistivity. Such dependence is often called non-Fermi liquid behavior and its origin was discussed. At higher temperatures (100-300K), mechanically alloyed Fe-Cu exhibited unusual T linear dependence resistivity. Such behavior is often called strange metallicity or non-fermi liquid behavior. The origin of such behavior was also discussed. Moreover, it was concluded that all the mechanically alloyed Fe-Cu are ferromagnetic in the measurement range of 2-350K. The

magnetization measured in a field of 0.5 T at 2K dropped monotonically from 195 emu/g to 55 emu/g from elemental Fe to Fe<sub>25</sub>Cu<sub>75</sub> alloy. In the materials investigated and based on the lattice parameters determined from the XRD, the volume per atom corresponds to a value of 12.13Å<sup>3</sup> for Fe<sub>50</sub>Cu<sub>50</sub> while it is 12.17Å<sup>3</sup> for Fe<sub>25</sub>Cu<sub>75</sub>. All the estimated volumes for the alloy system suggest a high-volume state consistent with Weiss model predictions of the ferromagnetic ground state.

Following the analysis of the Fe<sub>x</sub>Cu<sub>100-x</sub> system, the Fe<sub>50</sub>Cu<sub>50</sub> was selected for further evaluation as potential counter electrode in DSSC due to its low resistivity compared to the remaining Fe-Cu compositions. Fe<sub>50</sub>Cu<sub>50</sub> was deposited onto aluminum sheets and pressed using the rolling method to ensure contact between the powder and the conductive substrate (aluminum). This system was selected specifically due to its cost-effectiveness. The cells were produced, and then tested according to the IEC 60904-3:2008 Standard.

The cells were tested using platinum electrodes to obtain a reliable baseline. The Al-Fe<sub>50</sub>Cu<sub>50</sub> counter electrode was tested before and after rolling the aluminum sheet. It was observed that rolling the aluminum sheets impacted the results significantly. The performance of the cells using both platinum electrode and rolled Al-Fe<sub>50</sub>Cu<sub>50</sub> counter electrode were discussed. The current-voltage and power-voltage curves of a representative cell were evaluated using platinum electrode and rolled Al-Fe<sub>50</sub>Cu<sub>50</sub> counter electrode. The platinum electrode yielded an efficiency =2.91%, FF=62.1%, Voc=0.71V, Isc=6.60mA, and Pmax=0.728mW. On the other hand, the use of Al-Fe<sub>50</sub>Cu<sub>50</sub> counter electrode resulted in an efficiency=0.129%, FF=28.5%, Voc=0.28V, Isc 1.64mA, and Pmax=0.032mW. Additionally, the drop in trend was discussed, and possible solutions were suggested to improve the Al-Fe<sub>50</sub>Cu<sub>50</sub> counter electrode's performance.

Since the Fe<sub>50</sub>Cu<sub>50</sub> alloy was selected in this work as a potential cost-effective alternative for the rather expensive platinum, the results obtained from both counter-electrodes were compared, in terms of efficiency (%), total cell cost (AED), and normalized efficiency (% / AED). Although the efficiency was relatively low compared to that of the platinum electrode, the cost invested into the electrode was relatively low. This was further highlighted by the comparing the efficiency-levels normalized by the corresponding cell cost. The results, conducted analysis, and comparisons point to the

great potential of the Fe-Cu system which warrants further research and optimization efforts.

## References

- [1] United Nations, “World Population Prospects 2019: Highlights,” 2019. [https://www.un.org/development/desa/pd/sites/www.un.org.development.desa.pd/files/files/documents/2020/Jan/wpp2019\\_highlights.pdf](https://www.un.org/development/desa/pd/sites/www.un.org.development.desa.pd/files/files/documents/2020/Jan/wpp2019_highlights.pdf) (accessed: Jun. 23, 2020).
- [2] “Population, total - World | Data.” <https://data.worldbank.org/indicator/SP.POP.TOTL?locations=1W> (accessed Jun. 23, 2020).
- [3] “Welcome to the 3rd Industrial Revolution.” <https://magazine.wharton.upenn.edu/issues/summer-2015/welcome-to-the-third-industrial-revolution/> (accessed Jun. 23, 2020).
- [4] Y. A. Ul'yanin, V. V. Kharitonov, and D. Y. Yurshina, “Forecasting the Dynamics of the Depletion of Conventional Energy Resources,” *Studies on Russian Economic Development*, vol. 29, no. 2, pp. 153–160, Mar. 2018, doi: 10.1134/S1075700718020156.
- [5] A. da Rosa, *Fundamentals of Renewable Energy Processes*. Elsevier, 2009. doi: 10.1016/B978-0-12-374639-9.X0001-2.
- [6] E. A. News, “Mohammed bin Rashid launches world’s largest AED14.2bn Concentrated Solar Power plant,” 2017. <http://wam.ae/en/details/1395302632873> (accessed Nov. 14, 2020).
- [7] L. Phillips, “Solar energy,” in *Managing Global Warming: An Interface of Technology and Human Issues*, Elsevier, 2018, pp. 317–332. doi: 10.1016/B978-0-12-814104-5.00009-0.
- [8] “Solar energy - The Official Portal of the UAE Government.” <https://u.ae/en/information-and-services/environment-and-energy/water-and-energy/types-of-energy-sources/solar-energy> (accessed Nov. 14, 2020).
- [9] B. O'Regan and M. Grätzel, “A low-cost, high-efficiency solar cell based on dye-sensitized colloidal TiO<sub>2</sub> films,” *Nature*, vol. 353, no. 6346, pp. 737–740, Oct. 1991, doi: 10.1038/353737a0.
- [10] National Renewable Energy Laboratory, “Best Research-Cell Efficiencies,” Jun. 2021. <https://www.nrel.gov/pv/assets/pdfs/best-research-cell-efficiencies.20200104.pdf> (accessed Jun. 10, 2021).
- [11] Q. Ma, Z. Jia, L. Meng, J. Zhang, H. Zhang, W. Huang, J. Yuan, F. Gao, Y. Wan, Z. Zhang, and Y. Li, “Promoting charge separation resulting in ternary organic solar cells efficiency over 17.5%,” *Nano Energy*, vol. 78, no. July, p. 105272, Dec. 2020, doi: 10.1016/j.nanoen.2020.105272.
- [12] A. Bartolotta and G. Calogero, “Dye-sensitized solar cells: From synthetic dyes to natural pigments,” in *Solar Cells and Light Management: Materials, Strategies and Sustainability*, 1st ed., Elsevier, 2019, pp. 107–161. doi: 10.1016/B978-0-08-102762-2.00004-5.
- [13] L. C. Chen and C. J. Huang, “Optoelectronic properties of dye-sensitized solar cells with electroplated graphene electron transport layer,” *Materials Science in Semiconductor Processing*, vol. 35, pp. 162–165, 2015, doi: 10.1016/j.mssp.2015.03.008.
- [14] S. Nachimuthu, K.-H. Lai, F. Taufany, and J.-C. Jiang, “Theoretical study on molecular design and optical properties of organic sensitizers,” *Physical Chemistry Chemical Physics*, vol. 16, no. 29, p. 15389, 2014, doi: 10.1039/c4cp01653j.
- [15] X. Liu, J. M. Cole, P. G. Waddell, T. C. Lin, J. Radia, and A. Zeidler, “Molecular

- origins of optoelectronic properties in coumarin dyes: Toward designer solar cell and laser applications,” *Journal of Physical Chemistry A*, vol. 116, no. 1, pp. 727–737, 2012, doi: 10.1021/jp209925y.
- [16] K. Hara *et al.*, “Oligothiophene-Containing Coumarin Dyes for Efficient Dye-Sensitized Solar Cells,” *The Journal of Physical Chemistry B*, vol. 109, no. 32, pp. 15476–15482, Aug. 2005, doi: 10.1021/jp0518557.
- [17] T. Horiuchi, H. Miura, K. Sumioka, and S. Uchida, “High Efficiency of Dye-Sensitized Solar Cells Based on Metal-Free Indoline Dyes,” *Journal of the American Chemical Society*, vol. 126, no. 39, pp. 12218–12219, Oct. 2004, doi: 10.1021/ja0488277.
- [18] J. Theerthagiri, A. R. Senthil, J. Madhavan, and T. Maiyalagan, “Recent Progress in Non-Platinum Counter Electrode Materials for Dye-Sensitized Solar Cells,” *ChemElectroChem*, vol. 2, no. 7, pp. 928–945, Jul. 2015, doi: 10.1002/celec.201402406.
- [19] S. E. Kooops, P. R. F. Barnes, B. C. O’Regan, and J. R. Durrant, “Kinetic competition in a coumarin dye-sensitized solar cell: Injection and recombination limitations upon device performance,” *Journal of Physical Chemistry C*, vol. 114, no. 17, pp. 8054–8061, May 2010, doi: 10.1021/jp910972x.
- [20] U. Ahmed, M. Alizadeh, N. A. Rahim, S. Shahabuddin, M. S. Ahmed, and A. Pandey, “A comprehensive review on counter electrodes for dye sensitized solar cells: A special focus on Pt-TCO free counter electrodes,” *Solar Energy*, vol. 174, pp. 1097–1125, Nov. 2018, doi: 10.1016/j.solener.2018.10.010.
- [21] J. Briscoe and S. Dunn, “The Future of Using Earth-Abundant Elements in Counter Electrodes for Dye-Sensitized Solar Cells,” *Advanced Materials*, vol. 28, no. 20, pp. 3802–3813, May 2016, doi: 10.1002/adma.201504085.
- [22] K. H. Moyer, M. J. McDermott, M. J. Topolski, and D. F. Kearney, “Magnetic properties of iron alloys,” *Powder Technology*, vol. 30, no. 1, pp. 51–71, Sep. 1981, doi: 10.1016/0032-5910(81)85026-7.
- [23] S. K. Bose, O. V Dolgov, J. Kortus, O. Jepsen, and O. K. Andersen, “Pressure dependence of electron-phonon coupling and superconductivity in HCP Fe: A linear response study,” *Physical Review B - Condensed Matter and Materials Physics*, vol. 67, no. 21, p. 214518, Jun. 2003, doi: 10.1103/PhysRevB.67.214518.
- [24] K. Shimizu *et al.*, “Superconductivity in the non-magnetic state of iron under pressure,” *Nature*, vol. 412, no. 6844, pp. 316–318, Jul. 2001, doi: 10.1038/35085536.
- [25] K. Fukamichi, “Magnetovolume effects in amorphous alloys,” *Amorphous Metallic Alloys*, pp. 317–340, Jan. 1983, doi: 10.1016/B978-0-408-11030-3.50022-4.
- [26] P. Gorria *et al.*, “Invar effect in fcc-FeCu solid solutions,” *Physical Review B - Condensed Matter and Materials Physics*, vol. 69, no. 21, pp. 1–5, 2004, doi: 10.1103/PhysRevB.69.214421.
- [27] F. Heringhaus and D. Raabe, “Recent advances in the manufacturing of copper-base composites,” *Journal of Materials Processing Technology*, vol. 59, no. 4, pp. 367–372, Jun. 1996, doi: 10.1016/0924-0136(95)02179-5.
- [28] M. Ferry, “Alloys: Iron,” in *Reference Module in Materials Science and Materials Engineering*, Elsevier, 2016, pp. 1–11. doi: 10.1016/B978-0-12-803581-8.01117-6.
- [29] A. H. Alami and A. A. Hawili, “Fe-Cu Metastable Alloy,” in *Reference Module*

- in Materials Science and Materials Engineering*, Elsevier, 2020. doi: 10.1016/B978-0-12-815732-9.00022-X.
- [30] C. L. Chien *et al.*, “Magnetic properties of  $\text{Fe}_x\text{Cu}_{100-x}$  solid solutions,” *Physical Review B*, vol. 33, no. 5, pp. 3247–3250, 1986, doi: 10.1103/PhysRevB.33.3247.
- [31] V. M. T. S. Barthem, R. D. Noce, W. A. A. Macedo, and D. Givord, “Magnetic properties of electrodeposited Fe-poor Fe-Cu alloys,” *Brazilian Journal of Physics*, vol. 39, no. 1A, pp. 182–185, 2009, doi: 10.1590/S0103-97332009000200010.
- [32] D. Martínez-Blanco, P. Gorria, M. J. Pérez, J. A. Blanco, and M. A. González, “Low temperature neutron diffraction and magnetization of  $\text{Fe}_{25}\text{Cu}_{75}$  solid solutions,” *Journal of Non-Crystalline Solids*, vol. 353, no. 8–10, pp. 859–861, 2007, doi: 10.1016/j.jnoncrysol.2006.12.115.
- [33] J. S. Benjamin, “Dispersion Strengthened Superalloys by Mechanical Alloying,” 1970.
- [34] J. S. Benjamin and T. E. Volin, “The mechanism of mechanical alloying,” *Metallurgical Transactions*, vol. 5, no. 8, pp. 1929–1934, Aug. 1974, doi: 10.1007/BF02644161.
- [35] C. Suryanarayana, “Mechanical alloying and milling,” *Progress in Materials Science*, vol. 46, no. 1–2. Pergamon, pp. 1–184, Jan. 01, 2001. doi: 10.1016/S0079-6425(99)00010-9.
- [36] C. Suryanarayana, “Mechanical Alloying: A Novel Technique to Synthesize Advanced Materials,” *Research*, vol. 2019, pp. 1–17, 2019, doi: 10.34133/2019/4219812.
- [37] M. Rabiee, H. Mirzadeh, and A. Ataie, “Processing of Cu-Fe and Cu-Fe-SiC nanocomposites by mechanical alloying,” *Advanced Powder Technology*, vol. 28, no. 8, pp. 1882–1887, Aug. 2017, doi: 10.1016/j.apt.2017.04.023.
- [38] B.-L. Huang, R. J. Perez, E. J. Lavernia, and M. J. Luton, “Formation of supersaturated solid solutions by mechanical alloying,” *Nanostructured Materials*, vol. 7, no. 1–2, pp. 67–79, Jan. 1996, doi: 10.1016/0965-9773(95)00299-5.
- [39] M. F. Carrasco, S. K. Mendiratta, and L. Marques, “Formation of an intermediate phase in the ball milling synthesis of the sillenite phase of BSO and BTO,” *Applied Physics A: Materials Science and Processing*, vol. 80, no. 2, pp. 361–367, Feb. 2005, doi: 10.1007/s00339-003-2231-4.
- [40] V. V Tcherdyntsev *et al.*, “Al-Cu-Fe QUASICRYSTALLINE PHASE FORMATION BY MECHANICAL ALLOYING,” vol. 17, no. 6, pp. 825–841, 2002, doi: 10.1081/AMP-120016060.
- [41] L. Schultz, “Formation of amorphous metals by mechanical alloying,” *Materials Science and Engineering*, vol. 97, no. C, pp. 15–23, Jan. 1988, doi: 10.1016/0025-5416(88)90004-3.
- [42] M. Vaidya, G. M. Muralikrishna, and B. S. Murty, “High-entropy alloys by mechanical alloying: A review,” *Journal of Materials Research*, vol. 34, no. 5, pp. 664–686, Mar. 2019, doi: 10.1557/jmr.2019.37.
- [43] S. Dubey, J. N. Sarvaiya, and B. Seshadri, “Temperature Dependent Photovoltaic (PV) Efficiency and Its Effect on PV Production in the World A Review,” *Swapnil Dubey et al. / Energy Procedia*, vol. 33, pp. 311–321, 2013, doi: 10.1016/j.egypro.2013.05.072.
- [44] L. Qu *et al.*, “Studies of electrical resistivity of an annealed Cu-Fe composite,”

- Journal of Applied Physics*, vol. 113, no. 17, pp. 1–6, 2013, doi: 10.1063/1.4803716.
- [45] J. D. Verhoeven, S. C. Chueh, and E. D. Gibson, “Strength and conductivity of in situ Cu-Fe alloys,” *Journal of Materials Science*, vol. 24, no. 5, pp. 1748–1752, May 1989, doi: 10.1007/BF01105700.
- [46] S. Nachimuthu, W.-C. Chen, E. G. Leggesse, and J.-C. Jiang, “First principles study of organic sensitizers for dye sensitized solar cells: effects of anchoring groups on optoelectronic properties and dye aggregation,” *Physical Chemistry Chemical Physics*, vol. 18, no. 2, pp. 1071–1081, 2016, doi: 10.1039/C5CP04877J.
- [47] J. K. Roy, S. Kar, and J. Leszczynski, “Insight into the optoelectronic properties of designed solar cells efficient tetrahydroquinoline dye-sensitizers on TiO<sub>2</sub> (101) surface: first principles approach,” *Scientific Reports*, vol. 8, p. 10997, 2018, doi: 10.1038/s41598-018-29368-9.
- [48] A. H. Alami, K. Aokal, and M. Faraj, “Investigating nickel foam as photoanode substrate for potential dye-sensitized solar cells applications,” *Energy*, vol. 211, p. 118689, Nov. 2020, doi: 10.1016/j.energy.2020.118689.
- [49] G. Sahu, K. Wang, S. W. Gordon, W. Zhou, and M. A. Tarr, “Core-shell Au-TiO<sub>2</sub> nanoarchitectures formed by pulsed laser deposition for enhanced efficiency in dye sensitized solar cells,” *RSC Advances*, vol. 2, no. 9, pp. 3791–3800, 2012, doi: 10.1039/c2ra01030e.
- [50] M. Law, L. E. Greene, J. C. Johnson, R. Saykally, and P. Yang, “Nanowire dye-sensitized solar cells,” *Nature Materials*, vol. 4, no. 6, pp. 455–459, 2005. doi: 10.1038/nmat1387.
- [51] R. Lindsey, “Climate Change: Atmospheric Carbon Dioxide | NOAA Climate.gov.” <https://www.climate.gov/news-features/understanding-climate/climate-change-atmospheric-carbon-dioxide> (accessed Nov. 14, 2020).
- [52] Our World in Data, “Global primary energy consumption.” <https://ourworldindata.org/grapher/global-primary-energy> (accessed Jun. 23, 2020).
- [53] M. Denchak, “Fossil Fuels: The Dirty Facts | NRDC,” *Natural Resources Defense Council*, 2018. <https://www.nrdc.org/stories/fossil-fuels-dirty-facts> (accessed Jun. 23, 2020).
- [54] International Energy Agency, “Global CO<sub>2</sub> emissions in 2019 – Analysis - IEA.” <https://www.iea.org/articles/global-co2-emissions-in-2019> (accessed Jun. 23, 2020).
- [55] C. Figueres *et al.*, “Emissions are still rising: ramp up the cuts,” *Nature*, vol. 564, no. 7734. Nature Research, pp. 27–30, Dec. 06, 2018. doi: 10.1038/d41586-018-07585-6.
- [56] National Aeronautics and Space Administration (NASA), “2018 fourth warmest year in continued warming trend, according to NASA, NOAA – Climate Change: Vital Signs of the Planet.” <https://climate.nasa.gov/news/2841/2018-fourth-warmest-year-in-continued-warming-trend-according-to-nasa-noaa/> (accessed Jun. 23, 2020).
- [57] P. Fonta, “The ‘Paris agreement’ on climate change: An opportunity for cement sector to further reduce its CO<sub>2</sub> emissions,” in *Conference Proceedings - IEEE-IAS/PCA Cement Industry Technical Conference*, Jun. 2017, vol. 2017-May. doi: 10.1109/CITCON.2017.7951864.
- [58] Natural Resources Defense Council, “Paris Climate Agreement: Everything You



- Need to Know,” *Nrdc*, 2018. <https://www.nrdc.org/stories/paris-climate-agreement-everything-you-need-know> (accessed Jun. 23, 2020).
- [59] “World Energy Primary Production | Energy Production | Enerdata,” *Global Energy Statistical Yearbook 2020*. <https://yearbook.enerdata.net/total-energy/world-energy-production.html> (accessed Nov. 14, 2020).
- [60] “World Energy Consumption Statistics | Enerdata,” *Global Energy Statistical Yearbook 2020*. <https://yearbook.enerdata.net/total-energy/world-consumption-statistics.html> (accessed Nov. 14, 2020).
- [61] A. McCrone, U. Moslener, F. D’Estais, C. Grüning, and M. Emmerich, “Global Trends in Renewable Energy,” *Frankfurt School UNEP Centre*, vol. 1, no. 40, p. 80, 2020, doi: 10.24025/2306-4420.1.40.2015.84456.
- [62] “Global Solar Atlas.” <https://globalsolaratlas.info/detail?r=ARE&c=24.361644,53.9583,7> (accessed Nov. 15, 2020).
- [63] “Photovoltaic Power Potential - United Arab Emirates.” <https://globalsolaratlas.info/download/united-arab-emirates> (accessed Nov. 15, 2020).
- [64] E. Becquerel, “Report on the electrical effects produced under the influence of solar rays.” Accessed: Nov. 15, 2020. [Online]. Available: <https://www.ipvf.fr/>
- [65] “Becquerel Prize for Outstanding Merits in Photovoltaics: Alexandre Edmond Becquerel.” <https://www.becquerel-prize.org/about-the-becquerel-prize/alexandre-edmond-becquerel/> (accessed Nov. 15, 2020).
- [66] P. Wolfe, “What Is Photovoltaics?,” in *The Solar Generation*, Hoboken, NJ, USA: John Wiley & Sons, Inc., 2018, pp. 9–24. doi: 10.1002/9781119425618.ch2.
- [67] T. Markvart and L. Castañer, “Principles of Solar Cell Operation,” in *Solar Cells*, Elsevier Ltd, 2013, pp. 3–25. doi: 10.1016/B978-0-12-386964-7.00001-9.
- [68] S. Ananthakumar, J. R. Kumar, and S. M. Babu, “Third-Generation Solar Cells: Concept, Materials and Performance - An Overview,” in *Emerging Nanostructured Materials for Energy and Environmental Science*, S. Rajendran, M. Naushad, K. Raju, and R. Boukherroub, Eds. Cham: Springer International Publishing, 2019, pp. 4–6. doi: 10.1007/978-3-030-04474-9\_7.
- [69] A. Jain and A. Kapoor, “Exact analytical solutions of the parameters of real solar cells using Lambert W-function,” *Solar Energy Materials and Solar Cells*, vol. 81, no. 2, pp. 269–277, Feb. 2004, doi: 10.1016/j.solmat.2003.11.018.
- [70] Y. H. Hu and W. Wei, “Dye-Sensitized Materials,” in *Comprehensive Energy Systems*, vol. 2–5, Elsevier Inc., 2018, pp. 150–181. doi: 10.1016/B978-0-12-809597-3.00216-9.
- [71] S. Almosni *et al.*, “Material challenges for solar cells in the twenty-first century: directions in emerging technologies,” *Science and Technology of Advanced Materials*, vol. 19, no. 1, pp. 336–369, 2018, doi: 10.1080/14686996.2018.1433439.
- [72] W. Shockley and H. J. Queisser, “Detailed Balance Limit of Efficiency of p-n Junction Solar Cells,” *Electrical Power Journal of Applied Physics*, vol. 32, p. 4494, 1961, doi: 10.1063/1.1736034.
- [73] G. Conibeer, “Third-generation photovoltaics,” 2007.
- [74] I. Hussain, H. P. Tran, J. Jaksik, J. Moore, N. Islam, and M. J. Uddin, “Functional materials, device architecture, and flexibility of perovskite solar cell,” *Emergent Materials*, vol. 1, no. 3–4, pp. 133–154, 2018, doi: 10.1007/s42247-018-0013-1.

- [75] H. Goodwin, T. C. Jellicoe, N. J. L. K. Davis, and M. L. Böhm, “Multiple exciton generation in quantum dot-based solar cells,” *Nanophotonics*, vol. 7, no. 1. pp. 111–126, Jan. 01, 2018. doi: 10.1515/nanoph-2017-0034.
- [76] R. Garg, N. K. Dutta, and N. R. Choudhury, “Work Function Engineering of Graphene,” *Nanomaterials*, vol. 4, pp. 267–300, 2014, doi: 10.3390/nano4020267.
- [77] B. Kang, S. Lim, W. H. Lee, S. B. Jo, and K. Cho, “Work-function-tuned reduced graphene oxide via direct surface functionalization as source/drain electrodes in bottom-contact organic transistors,” *Advanced Materials*, vol. 25, no. 41, pp. 5856–5862, Nov. 2013, doi: 10.1002/adma.201302358.
- [78] J. Ajayan, D. Nirmal, P. Mohankumar, M. Saravanan, M. Jagadesh, and L. Arivazhagan, “A review of photovoltaic performance of organic/inorganic solar cells for future renewable and sustainable energy technologies,” *Superlattices and Microstructures*, vol. 143, no. May, p. 106549, 2020, doi: 10.1016/j.spmi.2020.106549.
- [79] N. S. Sariciftci, L. Smilowitz, A. J. Heeger, and F. Wudl, “Photoinduced electron transfer from a conducting polymer to buckminsterfullerene,” *Science*, vol. 258, no. 5087, pp. 1474–1476, 1992, doi: 10.1126/science.258.5087.1474.
- [80] W. Wang *et al.*, “Device characteristics of CZTSSe thin-film solar cells with 12.6% efficiency,” *Advanced Energy Materials*, vol. 4, no. 7, 2014, doi: 10.1002/aenm.201301465.
- [81] T. Gokmen, O. Gunawan, T. K. Todorov, and D. B. Mitzi, “Band tailing and efficiency limitation in kesterite solar cells,” *Applied Physics Letters*, vol. 103, no. 10, p. 103506, 2013, doi: 10.1063/1.4820250.
- [82] K. W. J. Barnham and G. Duggan, “A new approach to high-efficiency multibandgap solar cells A new approach to high~efficiency multi-band-gap solar cells,” *Citation: J. Appl. Phys*, vol. 67, p. 3490, 1990, doi: 10.1063/1.345339.
- [83] M. Hao *et al.*, “Ligand-assisted cation-exchange engineering for high-efficiency colloidal Cs<sub>1-x</sub>FaxPbI<sub>3</sub> quantum dot solar cells with reduced phase segregation,” *Nature Energy*, vol. 5, no. 1. pp. 79–88, 2020. doi: 10.1038/s41560-019-0535-7.
- [84] A. Kojima, K. Teshima, Y. Shirai, and T. Miyasaka, “Organometal halide perovskites as visible-light sensitizers for photovoltaic cells,” *Journal of the American Chemical Society*, vol. 131, no. 17, pp. 6050–6051, 2009, doi: 10.1021/ja809598r.
- [85] S. N. R. Kantareddy *et al.*, “Perovskite PV-Powered RFID: Enabling Low-Cost Self-Powered IoT Sensors,” *IEEE Sensors Journal*, vol. 20, no. 1, pp. 471–478, Jan. 2020, doi: 10.1109/JSEN.2019.2939293.
- [86] P. A. Serena and N. García, “Ferromagnetism in FeCu metastable alloys,” *Physical Review B*, vol. 50, no. 2, pp. 944–948, 1994, doi: 10.1103/PhysRevB.50.944.
- [87] E. H. P. . J. Wijn, *Magnetic Properties of Metals, d-Elements, Alloys and Compunds*. Springer-Verlag Berlin Heidelberg GmbH, 1967.
- [88] T. Kimura and Y. Otani, “Large spin accumulation in a permalloy-silver lateral spin valve,” *Physical Review Letters*, vol. 99, no. 19, pp. 1–4, 2007, doi: 10.1103/PhysRevLett.99.196604.
- [89] Z. Sun, M. Reisner, P. Fierlinger, A. Schnabel, S. Stuibler, and L. Li, “Dynamic modeling of the behavior of permalloy for magnetic shielding,” *Journal of*

- Applied Physics*, vol. 119, no. 19, 2016, doi: 10.1063/1.4949516.
- [90] C. Chang, B. Shen, and A. Inoue, “FeNi-based bulk glassy alloys with superhigh mechanical strength and excellent soft-magnetic properties,” *Applied Physics Letters*, vol. 89, no. 5, pp. 2004–2007, 2006, doi: 10.1063/1.2266702.
- [91] C. Rizal and B. B. Niraula, “Ferromagnetic alloys: Magnetoresistance, microstructure, magnetism, and beyond (review),” *Journal of Nano- and Electronic Physics*, vol. 7, no. 4, 2015, Accessed: Jun. 12, 2021. [Online]. Available: [https://www.researchgate.net/profile/Conrad-Rizal/publication/286929503\\_Ferromagnetic\\_Alloys\\_Magnetoresistance\\_Microstructure\\_Magnetism\\_and\\_Beyond\\_Review/links/5682447f08ae051f9aecf5bb/Ferromagnetic-Alloys-Magnetoresistance-Microstructure-Magnetism-and-Be](https://www.researchgate.net/profile/Conrad-Rizal/publication/286929503_Ferromagnetic_Alloys_Magnetoresistance_Microstructure_Magnetism_and_Beyond_Review/links/5682447f08ae051f9aecf5bb/Ferromagnetic-Alloys-Magnetoresistance-Microstructure-Magnetism-and-Be)
- [92] A. R. Yavari, P. J. Desré, and T. Benameur, “Mechanically driven alloying of immiscible elements,” *Physical Review Letters*, vol. 68, no. 14, pp. 2235–2238, Apr. 1992, doi: 10.1103/PhysRevLett.68.2235.
- [93] E. Ma, M. Atzmon, and F. E. Pinkerton, “Thermodynamic and magnetic properties of metastable FeCu 100-x solid solutions formed by mechanical alloying,” *Journal of Applied Physics*, vol. 74, no. 2, pp. 955–962, 1993, doi: 10.1063/1.354837.
- [94] J. Huang and J. Jiang, “Kinetic process of mechanical alloying,” *Physical Review B - Condensed Matter and Materials Physics*, vol. 58, no. 18, pp. R11817–R11820, 1998, doi: 10.1103/PhysRevB.58.R11817.
- [95] D. Sivaprahasam, A. M. Sriramamurthy, M. Vijayakumar, G. Sundararajan, and K. Chattopadhyay, “Synthesis of FeCu Nanopowder by Levitational Gas Condensation Process”, doi: 10.1007/s11663-010-9370-8.
- [96] R. D. Noce *et al.*, “Magnetic properties of Fe-Cu alloys prepared by pulsed electrodeposition,” *Journal of Applied Physics*, vol. 106, no. 9, 2009, doi: 10.1063/1.3253725.
- [97] P. Gorria *et al.*, “High-temperature induced ferromagnetism on  $\gamma$ -Fe precipitates in FeCu solid solutions,” *Physical Review B - Condensed Matter and Materials Physics*, vol. 72, no. 1, pp. 1–7, 2005, doi: 10.1103/PhysRevB.72.014401.
- [98] M. Eisenbach and G. M. Stocks, “Invar effect and noncollinear magnetism in FeCu alloys,” *Journal of Applied Physics*, vol. 105, no. 7, pp. 8–11, 2009, doi: 10.1063/1.3063070.
- [99] J. L. Gilbert, “Metals: Basic Principles,” in *Biomaterials Science*, Elsevier, 2020, pp. 205–227. doi: 10.1016/B978-0-12-816137-1.00017-9.
- [100] S. Subramanaya, “Diffusional Transformations,” in *Pergamon Materials Series*, vol. 12, 2007, pp. 555–716. doi: 10.1016/S1470-1804(07)80060-5.
- [101] M. Perez *et al.*, “Low Temperature Solubility of Copper in Iron : Experimental Study Using Thermoelectric Power, Small Angle X-ray Scattering and Tomographic Atom Probe Characterization of metallic weld parts View project Low-temperature solubility of copper in iron: experimental study using thermoelectric power, small angle X-ray scattering and tomographic atom probe,” *Philosophical Magazine*, vol. 85, no. 20, pp. 2197–2210, 2005, doi: 10.1080/14786430500079645.
- [102] Y.-Y. Chuang, R. Schmid, and Y. A. Chang, “Thermodynamic Analysis of the Iron-Copper System I” The Stable and Metastable Phase Equilibria,”
- [103] A. H. Alami and A. A. Hawili, “Synthesis, characterization and applications of FeCu alloys,” *Applied Surface Science Advances*, vol. 1, p. 100027, Nov. 2020, doi: 10.1016/j.apsadv.2020.100027.

- [104] A. H. Alami, M. A. Abdelkareem, M. Faraj, K. Aokal, and N. Al Safarini, “Titanium dioxide-coated nickel foam photoelectrodes for direct urea fuel cell applications,” *Energy*, vol. 208, p. 118253, Oct. 2020, doi: 10.1016/j.energy.2020.118253.
- [105] P. Gorria, D. Martínez-Blanco, J. A. Blanco, M. J. Pérez, M. A. González, and J. Campo, “Magnetism and structure of Fe–Cu binary solid solutions obtained by high-energy ball milling,” *Physica B: Condensed Matter*, vol. 384, no. 1–2, pp. 336–340, Oct. 2006, doi: 10.1016/j.physb.2006.06.038.
- [106] T. Mashimo, X. Huang, X. Fan, K. Koyama, and M. Motokawa, “Slater-Pauling curve of Fe-Cu solid solution alloys,” *Physical Review B - Condensed Matter and Materials Physics*, vol. 66, no. 13, pp. 1–4, 2002, doi: 10.1103/PhysRevB.66.132407.
- [107] C. Y. Ho *et al.*, “Electrical Resistivity of Ten Selected Binary Alloy Systems,” *Journal of Physical and Chemical Reference Data*, vol. 12, no. 2, pp. 183–322, 1983, doi: 10.1063/1.555684.
- [108] E. Ma, “Alloys created between immiscible elements,” *Progress in Materials Science*, vol. 50, pp. 413–509, 2005, doi: 10.1016/j.pmatsci.2004.07.001.
- [109] J. H. Mooij, “Electrical conduction in concentrated disordered transition metal alloys,” *Physica Status Solidi (a)*, vol. 17, no. 2, pp. 521–530, 1973, doi: 10.1002/pssa.2210170217.
- [110] A. L. Kuzemsky, *Electronic transport in metallic systems and generalized kinetic equations*, vol. 25, no. 23–24. 2011. doi: 10.1142/S0217979211059012.
- [111] P. A. Lee and T. V. Ramakrishnan, “Disordered electronic systems,” *Reviews of Modern Physics*, vol. 57, no. 2, pp. 287–337, 1985, doi: 10.1103/RevModPhys.57.287.
- [112] T. R. Kirkpatrick and D. Belitz, “Generic non-Fermi-liquid behavior of the resistivity in magnets with ferromagnetic, helical, or skyrmionic order,” *Physical Review B*, vol. 97, no. 6, pp. 1–14, 2018, doi: 10.1103/PhysRevB.97.064411.
- [113] E. W. Huang, R. Sheppard, B. Moritz, and T. P. Devereaux, “Strange metallicity in the doped Hubbard model,” *Science*, vol. 366, no. 6468, pp. 987–990, 2019, doi: 10.1126/science.aau7063.
- [114] C. Proust, B. Vignolle, J. Levallois, S. Adachi, and N. E. Hussey, “Fermi liquid behavior of the in-plane resistivity in the pseudogap state of YBa<sub>2</sub>Cu<sub>4</sub>O<sub>8</sub>,” *Proceedings of the National Academy of Sciences of the United States of America*, vol. 113, no. 48, pp. 13654–13659, 2016, doi: 10.1073/pnas.1602709113.
- [115] H. Oike, Y. Suzuki, H. Taniguchi, Y. Seki, K. Miyagawa, and K. Kanoda, “Anomalous metallic behaviour in the doped spin liquid candidate  $\kappa$ -(ET)<sub>4</sub>Hg<sub>2</sub>.89Br<sub>8</sub>,” *Nature Communications*, vol. 8, no. 1, pp. 1–7, 2017, doi: 10.1038/s41467-017-00941-6.
- [116] E. H. Hwang and S. Das Sarma, “Linear-in-T resistivity in dilute metals: A Fermi liquid perspective,” *Physical Review B*, vol. 99, no. 8, pp. 1–18, 2019, doi: 10.1103/PhysRevB.99.085105.
- [117] P. K. Misra, “Superconductivity,” in *Physics of Condensed Matter*, Elsevier, 2012, pp. 451–486. doi: 10.1016/B978-0-12-384954-0.00014-1.
- [118] L. M. Sandratskii, “Noncollinear magnetism in itinerant-electron systems: Theory and applications,” *Advances in Physics*, vol. 47, no. 1, pp. 91–160, 1998, doi: 10.1080/000187398243573.
- [119] S. Khmelevskiy and P. Mohn, “First-principles investigation of ferromagnetism

- and Invar effect in fcc Fe-Cu alloys,” *Physical Review B - Condensed Matter and Materials Physics*, vol. 71, no. 14, pp. 1–7, 2005, doi: 10.1103/PhysRevB.71.144423.
- [120] R. J. Weiss, “The origin of the ‘invar’ effect,” *Proceedings of the Physical Society*, vol. 82, no. 2, pp. 281–288, Aug. 1963, doi: 10.1088/0370-1328/82/2/314.
- [121] Y. Hishiyama, Y. Kaburagi, and M. Inagaki, “Magnetoresistance,” in *Materials Science and Engineering of Carbon*, Elsevier, 2016, pp. 173–204. doi: 10.1016/B978-0-12-805256-3.00009-X.
- [122] A. A. Bright, “Negative magnetoresistance in pregraphitic carbons,” *Carbon*, vol. 17, no. 3, pp. 259–263, 1979, doi: 10.1016/0008-6223(79)90085-X.
- [123] K. Yazawa, “Negative Magneto-Resistance in Pyrolytic Carbons,” *Journal of the Physical Society of Japan*, vol. 26, no. 6, pp. 1407–1419, Jun. 1969, doi: 10.1143/JPSJ.26.1407.
- [124] H. Yamada and S. Takada, “Negative Magnetoresistance of Ferromagnetic Metals due to Spin Fluctuations,” *Progress of Theoretical Physics*, vol. 48, no. 6, pp. 1828–1848, 1972, doi: 10.1143/ptp.48.1828.
- [125] A. Berni, M. Mennig, and H. Schmidt, “doctor blade,” pp. 8–11, 1952.
- [126] A. H. M. Smets, K. Jäger, O. Isabella, R. A. van Swaaij, and M. Zeman, “Solar Cell Parameters and Equivalent Circuit,” *Solar energy: the physics and engineering of photovoltaic conversion, technologies and systems*, pp. 113–121, 2016, Accessed: Jul. 03, 2021. [Online]. Available: [https://ocw.tudelft.nl/wp-content/uploads/solar\\_energy\\_section\\_9\\_1\\_9\\_3.pdf](https://ocw.tudelft.nl/wp-content/uploads/solar_energy_section_9_1_9_3.pdf)
- [127] A. A. Bayod-Rújula, “Solar photovoltaics (PV),” 2019. doi: 10.1016/B978-0-12-814853-2.00008-4.
- [128] M. Chegaar, A. Hamzaoui, A. Namoda, P. Petit, M. Aillerie, and A. Herguth, “Effect of Illumination Intensity on Solar Cells Parameters,” *Energy Procedia*, vol. 36, pp. 722–729, 2013, doi: 10.1016/j.egypro.2013.07.084.
- [129] A. Hagfeldt *et al.*, “Dye-Sensitized Photoelectrochemical Cells,” 2011. doi: 10.1016/B978-0-12-385934-1.00015-5.
- [130] B. Tripathi, P. Yadav, and M. Kumar, “Effect of Varying Illumination and Temperature on Steady-State and Dynamic Parameters of Dye-Sensitized Solar Cell Using AC Impedance Modeling,” *International Journal of Photoenergy*, vol. 2013, 2013, doi: 10.1155/2013/646407.
- [131] J. B. Véchembre and G. R. Fox, “Sintering of screen-printed platinum thick films for electrode applications,” 2017, doi: 10.1557/JMR.2001.0131.
- [132] “Test Cell Spare Parts - Solaronix Online Shop.” <https://shop.solaronix.com/test-cell-spare-parts.html> (accessed Jun. 26, 2021).
- [133] “ALDRICH Copper, powder, <math>425\text{m}</math>, 99.5% trace metals basis.” [https://www.thomasci.com/Chemicals/Reagent-C/\\_/ALDRICH-Copper-powder-425m-995-trace-metals-basis](https://www.thomasci.com/Chemicals/Reagent-C/_/ALDRICH-Copper-powder-425m-995-trace-metals-basis) (accessed Jun. 26, 2021).
- [134] “ALDRICH Iron,  $\geq 99\%$ , powder (fine).” [https://www.thomasci.com/Chemicals/Reagent-I/\\_/ALDRICH-Iron-99-powder-fine](https://www.thomasci.com/Chemicals/Reagent-I/_/ALDRICH-Iron-99-powder-fine) (accessed Jun. 26, 2021).
- [135] “Aluminium Sheets - MIH HOME.” <https://mihhome.com/aluminium/aluminium-sheets/plain-sheets/> (accessed Jun. 26, 2021).
- [136] A. L. Hammond, “Photovoltaics: The Semiconductor Revolution Comes to Solar,” 1977.

## **Vita**

Mariam Yousif Y. AlAwadhi was born in 1997, in Dubai, in the United Arab Emirates. She graduated from Al Maarifa International Private School in 2014 in Sharjah and began her undergraduate studies in the University of Sharjah. During her junior year, she was the Women's Student Council President. In 2018, she graduated with a Bachelor of Science degree in Sustainable and Renewable Energy Engineering.

In 2019, Eng. AlAwadhi joined Dubai Police and worked in the field of Sustainability in policing entities. She was part of the United Nation Alliance for Civilization's (UNAOC) fourth edition of Young Peacebuilders. In 2020, she was a team leader in Dubai Police's strategic update.

Simultaneously, she began her Masters of Science in Mechanical Engineering at the American University of Sharjah in 2019. Eng. AlAwadhi is a part of the Dubai Police Scientists Council.